

Mechanical Properties of Polymer-Supported Reduced Graphene Oxide (rGO) Membranes

A Thesis

Presented to

The Academic Faculty

by

Hazel P. Dhruve

In Partial Fulfillment
of the Requirements for the Degree Master of Science in Materials Science and Engineering
in the School of Materials Science and Engineering

Georgia Institute of Technology

August 2024

Copyright © 2024 by Hazel P. Dhruve

Mechanical Properties of Polymer-Supported Reduced Graphene Oxide (rGO) Membranes

Approved by:

Dr. Meisha L. Shofner, Advisor

School of Materials Science and Engineering

Georgia Institute of Technology

Dr. Donggang Yao

School of Materials Science and Engineering

Georgia Institute of Technology

Dr. Sankar Nair

School of Chemical and Biomolecular Engineering

Georgia Institute of Technology

Date Approved: [July 5, 2024]

ACKNOWLEDGEMENTS

I would like to start by thanking my advisor, Dr. Meisha Shofner. She gave me the opportunity to be a part of her wonderful research group and she has been a constant support since then. Over the past two years, I have learned a lot from her. She has guided me every step of the way during my master's, while also being open to my ideas and suggestions. She has never been hesitant to spend time explaining new concepts to me, sometimes more than once. Her advice and kind words of motivation have helped me navigate my way through my thesis research. I look up to her dedication and her work ethic, and I am inspired to one day be half as brilliant as she is – thank you Dr. Shofner.

I would like to thank the members of my thesis committee – Dr. Sankar Nair and Dr. Donggang Yao. I appreciate you taking out the time for my thesis defense, and I am grateful for your valuable input and suggestions.

Next, I want to thank my lab group, Emily Ryan, Malik Blackman and Fariha Rubaiya, for being so kind and welcoming when I joined the group. I am grateful for their support and guidance, and for all the conversations that I have shared with them in between all the research. I want to thank Muskan Sonker, Kaung Su Khin Zaw, and Madeline Garell for being absolute team players, and for teaching me other interesting things about the project.

Next, I would like to thank the trainers at Georgia Tech who have helped me learn some truly fascinating instruments and have never failed to answer all of my questions – Mr. Walter Henderson for training me on the Hysitron Triboindenter, Mr. Tiejun Zhang for training me on the

Hitachi SEM, and Dr. Laxminarayanan Krishnan for training me on the small-scale tensile testing load frame.

I would like to thank my funding sources – the Department of Energy (DOE) Office of Energy Efficiency and Renewable Energy (DE-EE-0009496) who supported this work.

I want to thank my mentor, and my professor back home, Dr. S.T. Mhaske, for believing in me and for bringing out the best in me.

Finally, I would like to thank my friends and family. I want to start by thanking Vedant Gaikwad, for his unconditional support which has given me the strength to pursue my dreams. He has been there for me every single day, inspiring me to give my best. None of this would have been possible without him - thank you Vedant. I want to thank my parents for making me fearless and wishing the best for me. I would not have achieved the things I have today had it not been for my mother's sharing my love for books. I want to thank my grandmom for all her love, I miss her and I know she would have been proud of this day. Lastly, I am grateful to have found friends who I can call family. These include, but are not limited to - Rucha Chotalia, Bhavi Dave, Nandinee Kaushik, Yash Doshi, Ananya Agarwal, Preksha Vichare, Sumer Kadam, Sutikshan Bansal, Parin Shah, Sathyanarayan Sairam Jaishankar, Kavya Krishnan, and Aparna Ravi. I am grateful to have found a home away from home at Georgia Tech, and I will always cherish the time that I have spent here.

TABLE OF CONTENTS

ACKNOWLEDGEMENTS	iii
LIST OF TABLES	viii
LIST OF FIGURES	ix
LIST OF SYMBOLS AND ABBREVIATIONS	xiii
SUMMARY	xv
CHAPTER 1. INTRODUCTION	1
CHAPTER 2. BACKGROUND.....	4
2.1. Polymer membranes used for nanofiltration	4
2.2. Reduced graphene oxide (rGO) used in separation membranes	9
2.3. Intercalants used for separation membranes	14
2.4. Bridging the gap in literature.	16
CHAPTER 3: MATERIALS AND METHODS	18
3.1. Materials	18
3.2. Sample Preparation	19
3.2.1. Preparation of bare polymer supports (PES and PVDF), rGO-polymer membranes, rGO-X-polymer membranes, and their compacted counterparts	20

3.2.2. Preparation of wet membranes.....	24
3.2.3. Sample preparation for mechanical testing.....	25
3.2.4. Preparation of the free-standing rGO/rGO-X films.....	25
3.3. Measurement Principles and Methods.....	27
3.3.1. Scanning Electron Microscopy (SEM).....	27
3.3.2. Tensile Testing.....	28
3.3.3. Nanoindentation and High-Speed Nanoindentation.....	30
3.3.4. Tensile testing of FS films.....	34
3.3.5. Fragmentation Test.....	36
3.4. Modeling.....	39
CHAPTER 4. EFFECT OF COMPACTION AND WATER ON THE MECAHNICAL PROPERTIES OF PVDF SUPPORTED MEMBRANES.....	41
CHAPTER 5. COMPONENT EFFECT ON THE AXIAL AND TRANSVERSE MECHANICAL PROPERTIES OF THE DRY MEMBRANES.....	54
5.1. Effect of the substrate on the mechanical properties of the membranes.....	55
5.2. Effect of the intercalant on the mechanical properties of the membranes.....	59
5.3. Free-standing (FS) rGO/rGO-X films.....	62
5.3.1. Scanning electron micrographs of the FS films.....	63
5.3.2. Small-scale tensile testing of the FS films.....	66
5.3.3. Nanoindentation of the FS films.....	68
5.4 Modeling.....	70

5.5 Interfacial shear traction of the rGO/rGO-X layer on PES support.....	73
CHAPTER 6. CONCLUSION AND FUTURE WORK.....	77
6.1. Conclusion	77
6.2. Future Work.....	79
REFERENCES.....	81

LIST OF TABLES

Table 3.1 - List of membranes used in this work	20
Table 5.1 - The different structures and dimensions of the intercalants used with the PES supported membranes	60
Table 5.2 - Thickness values of the 50FS films obtained by cross-sectional SEM	66
Table 5.3 - The fracture stress and modulus values of the 50FS rGO/rGO-X films when tested in tension.	67
Table 5.4 - The E_r values obtained by nanoindentation of the upper and lower sides of the 50FS films and the 32FS films	69

LIST OF FIGURES

Figure 2.1	Characteristics of different types of pressure driven separation membranes	5
Figure 2.2	Materials that are commonly used to make nanofiltration membranes	6
Figure 2.3	A schematic showing the different layers of a thin-film composite nanofiltration membrane	7
Figure 2.4	Structure of PVDF	8
Figure 2.5	Structure of PES	9
Figure 2.6	Schematic showing the structure of graphene, GO and rGO	10
Figure 2.7	A schematic showing the Hummers method used to synthesize GO from graphene	11
Figure 2.8	A schematic showing how a typical graphene membrane works (for RO)	13
Figure 2.9	Stacked layers of free-standing rGO rejecting the salts during the desalination process.	14
Figure 2.10	A schematic showing the sieving effect and the tortuosity to the path of incoming water provided by the intercalated GO-polyamide membrane	16
Figure 2.11	Schematic of the polymer-supported rGO/rGO-X membrane used in this research	17
Figure 3.1	The steps involved in the fabrication of the membranes	23

Figure 3.2	Image of a 50FS rGO film.	26
Figure 3.3	Vacuum filtration set-up used to make the FS rGO/rGO-X films.	27
Figure 3.4	A typical stress-strain curve for a polymer film, showing the modulus, and the ultimate strength (or tensile strength). The area under this curve gives the toughness of the sample.	29
Figure 3.5	A typical loading-holding-unloading curve used in nanoindentation	32
Figure 3.6	Experimental set-up for nanoindentation- the membrane sample (highlighted by the red box), is held down by pins onto a cylinder which is stuck on the stage	33
Figure 3.7	Fragmented compacted rGO-AZ-3 at a magnification of 200x	38
Figure 3.8	Protocol for choosing different locations on the fragmented sample to ensure that the cracks are observed at the edge and the central locations systematically	39
Figure 4.1	Representative stress-strain curve for the dry, compacted PVDF membranes.	42
Figure 4.2	Modulus (a), tensile strength (b), toughness (c), and E_r (d) values for the non-compact and compacted PVDF membranes in the dry state	44
Figure 4.3	Force strain curves of the non-compact PVDF support and the crossflow-compact PVDF support.	49
Figure 4.4	The modulus (a), tensile strength (b), toughness (c), and E_r (d) values for the wet PVDF supported membranes having different loadings of TBO.	50

Figure 4.5	Force-strain curves of the non-compacted PVDF support and the PVDF support compacted with the hydraulic press.	52
Figure 5.1	Schematic showing the different components of the membrane	55
Figure 5.2	The cross-sectional SEM images of the PVDF polymer support (a), and the PES polymer support (b).	56
Figure 5.3	The modulus (a), tensile strength (b), toughness (c) and E_r (d) values for the dry PES supported membranes having different loadings of TBO	58
Figure 5.4	Force strain curves of the non-compacted PES support and the PES support compacted with the hydraulic press.	59
Figure 5.5	The modulus (a), tensile strength (b) and toughness (c) values, and the E_r values (d), for the PES supported membranes containing 9.1 wt.% loading of different intercalants.	62
Figure 5.6	Schematic showing the FS rGO/rGO-X film	63
Figure 5.7	The cross-sectional SEM images (a) and (b) of the 32FS rGO film	64
Figure 5.8	The cross-sectional SEM images of the 50FS rGO (a), rGO-Z-1 (b), rGO-TM-1 (c), rGO-AZ-3 (d), and rGO-AZ-1 (e) films.	65
Figure 5.9	Experimental set-up to test FS films under tension before testing (a), and after fracture (b)	66
Figure 5.10	Representative stress-strain curves for the 50FS films tested in tension.	68

Figure 5.11	The experimental values of E_c and how these values compare to the E_c values obtained by fitting the different models.	71
Figure 5.12	Schematic to show the interface between the rGo/rGO-X layer and the PES support.	73
Figure 5.13	The interfacial shear traction versus the non-compacted fragmented sample.	74

LIST OF SYMBOLS AND ABBREVIATIONS

α	Threshold of statistical significance
AZ-1	Bismarck Brown
AZ-3	Allura Red
β	Geometry Correction Factor
DI	Deionized
E	Young's modulus
E_r	Reduced Modulus
FL-1	Eosin-B
GO	Graphene oxide
H	Hardness
h	Thickness/maximum indentation depth
L	Liter
λ	Mean Spacing Between Cracks
m	Meter
N	Newtons
NF	Nanofiltration
OX-1	Gallocyanin
P_{max}	Peak Load applied by the nanoindenter
PC	Polycarbonate
PES	Polyethersulfone
PVA	Polyvinyl alcohol
PVDF	Polyvinylidene fluoride

rpm	Revolutions per minute
rGO	Reduced Graphene Oxide
RO	Reverse Osmosis
σ_{frac}	Fracture Stress
s	Second
TH	Thionin
TM-1	Crystal Violet
TMP	Transmembrane Pressure
TS	Total Solids
τ_{max}	Maximum Interfacial Shear Traction
TZ-1	Toluidine Blue O
TZ-2	Methylene Blue
TZ-3	Methylene Green
TZ-4	Thionin

SUMMARY

Sustainable innovations designed to save water are the need of the hour as the world is heading towards shortages of clean water. The impact of these innovations can be fully realized if they are feasible at an industrial level while contributing to the efficiency of the industrial process. With the goal of saving water and incorporating sustainability industrially, this research project is aimed at examining the mechanical performance of the materials used to make the membranes so that the mechanical properties can be correlated to the membrane performance.

The motivation for this research is to gain a thorough understanding of the mechanical properties of the polymer-supported membranes composed of reduced graphene oxide (rGO) or intercalated rGO (rGO-X). A sound knowledge of the mechanical properties, like the stiffness (modulus), transverse stiffness (reduced modulus or E_r), the adhesion strength of the rGO layer on polymer, and the effect of the membrane components, can help understand and improve the membrane performance. Free-standing rGO/rGO-X films were fabricated and tested to isolate the mechanical contribution of the thin rGO layer from the polymer support. Lastly, micromechanical models were used to predict the composite transverse modulus values of the membranes.

Some key observations made during this research project were that compaction improved the axial mechanical properties of the polyvinylidene fluoride (PVDF) based membranes whereas the introduction of water negated this improvement. The intercalants acted as pillars, reinforcing the membrane in the transverse direction. Moreover, the inverse rule of mixtures, and a modified version of it, estimated values close to the experimental composite transverse modulus values. Overall, the PVDF supported membranes were stiffer than their polyether sulfone (PES) counterparts. Tensile testing and nanoindentation of the free-standing films help elucidate that toluidine blue O and crystal violet were more robust as intercalants as compared to the azo dyes.

CHAPTER 1. INTRODUCTION

The desalting process of crude oil in the petroleum industry consumes an enormous amount of water to clean the crude oil [1]. The crude oil used in the petroleum industry can be contaminated with salts and these salts can harm the equipment by promoting corrosion and can negatively affect the downstream process catalysts. To wash away these salts before the distillation step, a desalting process is carried out wherein water is used to wash away the salts from the oil [2, 3]. According to the US Energy Information and Administration (EIA) report, 12.933 million barrels of crude oil were produced in the United States, per day, in 2023. A barrel contains close to 42 gallons of crude oil. Each gallon of crude oil requires about 1-1.9 gallons of water for desalting [4]. Thus, the amount of water consumed by this process, and this industry, is massive, thereby calling for improved water management.

To treat industrial wastewater, which is heavy in hydrocarbon content, organics and inorganics, a membrane system needs to be designed such that it can withstand these strong chemicals. Moreover, the membranes would have to be functional at high temperatures and pressures. To design such a membrane system, two polymers were explored as the supports – a fluorinated polymer, polyvinylidene fluoride (PVDF), and a sulfonated polymer, polyethersulfone (PES). Graphene, the 2D form of carbon, arranges in a stacked structure and is resistant to a variety of chemicals. The same properties are exhibited by reduced graphene oxide (rGO). The PES and PVDF polymers supported a thin layer of rGO which was about 130-170 nm in thickness. The rGO layer was further modified by using a drop-in additive, called an intercalant, and denoted by

‘X’. The rGO/rGO-X layer provided chemical stability, and a tortuous path to the incoming wastewater, thereby ensuring satisfactory rejection of the wastes to obtain relatively clean water.

This research project was focused on characterizing these membranes. Tensile testing was used to find the modulus, tensile strength and the toughness of the membranes. Nanoindentation and accelerated property mapping (HSN) were used to quantify the transverse stiffness of the membranes. Moreover, free-standing (FS) films were synthesized and tested using a small-scale tensile testing load frame, to find the mechanical contribution of the thin rGO/rGO-X layer independent of the polymer support. Modeling was used to predict the composite transverse modulus and compare the simulated values to the experimental ones. Finally, fragmentation testing was used to find the adhesion strength of the rGO/rGO-X layer on polymer. Multiple competing effects, like the processing conditions (compaction and hydration of the membranes), the interlayer spacing or the d-spacing, arrangement of the intercalant molecules – were all examined to provide an understanding of the membrane mechanical performance.

The subsequent chapters in this thesis are organized as follows: Chapter 2 provides a background on membrane separation and the rGO-polymer nanofiltration membranes used in this work; Chapter 3 gives information regarding the different materials and methods used in this project, along with the details for preparing the samples and the parameters used for modeling; Chapter 4 examines the effect of the processing conditions, compaction and hydration, on the mechanical properties of PVDF supported membranes, whereas Chapter 5 discusses the effect of changing the polymer support and using different intercalants. Chapter 5 also deals with the testing of the FS rGO/rGO-X films, and how the information obtained from these films complement the data obtained from the tensile and nanoindentation/HSN tests. Finally, Chapter 6 provides a holistic

view of the mechanical performance of the membranes and touches upon the future work of this project.

CHAPTER 2. BACKGROUND

This chapter aims to provide a broader context regarding the current landscape of rGO-polymer nanofiltration membranes, intercalants, and free-standing (FS) films so as to provide a background understanding in this area of research.

2.1. Polymer membranes used for nanofiltration. Membranes are materials that can act as a hindrance or obstruction for certain molecules, while allowing other molecules or ions or solvent to pass through. A simple way to imagine a membrane is to compare it to a sieve, wherein the membrane acts as ‘semi-permeable’ or ‘selective’, allowing only certain sizes of molecules or ions to pass through it, thereby displaying a sieving action [5]. Membranes can be classified based on how the transport of molecules or ions takes place through them – hydrostatic pressure, vapor pressure, concentration, or electrical potential can be the major driving forces for filtration [6]. For example, electrodialysis, developed in the 1950s to treat brackish water, uses a voltage source to drive the wastewater through cathodes and anodes to separate ions [7, 8]. Dialysis membranes, commonly employed in medicine, work on the principle that different concentrations on two sides of the membranes lead to the separation of molecules based on size [9]. Distillation is an example of a separation process driven by heat and thereby the vapor pressure created [10]. Microfiltration (MF), ultrafiltration (UF), nanofiltration (NF) and reverse osmosis (RO) are all examples of membrane separation processes which rely on hydraulic pressure. Nanofiltration membranes have pore sizes as small as 1 nm. These membranes have pore sizes that are between those for UF and RO membranes and are used industrially for a variety of applications like water softening, seawater desalination, biotechnology, textile water treatment, food and medical industries [11-15]. Figure 2.1 shows the different types of filtration processes and the associated pore size and application.

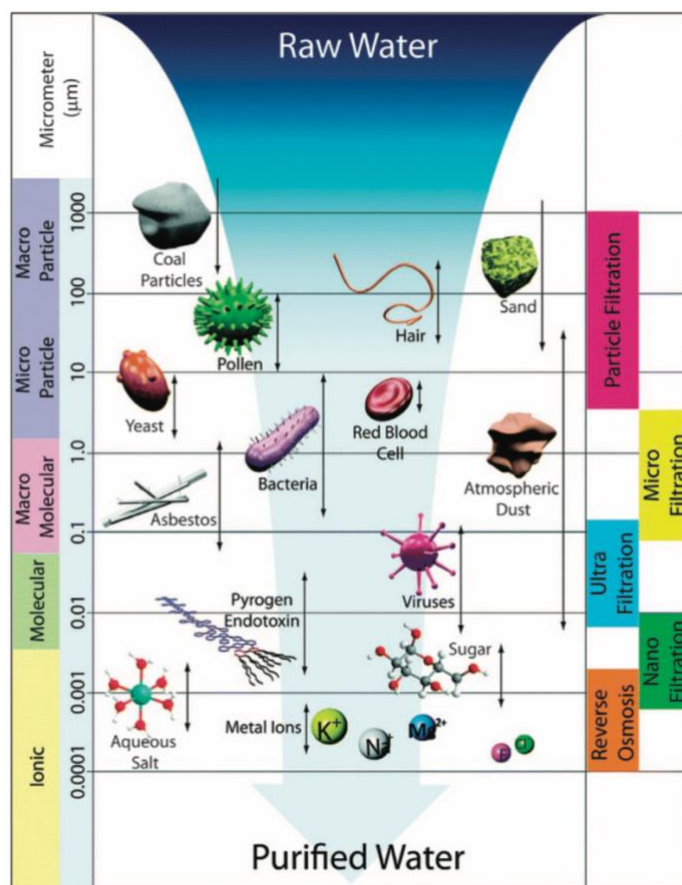


Figure 2.1: Characteristics of different types of pressure driven separation membranes [16].

Reprinted with permission. Copyright 2016, The Royal Society of Chemistry.

Nanofiltration is a pressure-driven filtration process, where the porous structure of the polymer provides a tortuous path for rejection of unwanted components from water. Two types of materials are predominantly used for nanofiltration membranes – ceramics [17] and polymers [18]. Figure 2.2 shows the commonly used materials to fabricate NF membranes. These materials can also be used to make RO membranes [19]. While ceramic membranes have better thermal stability than polymeric membranes, ceramic membranes tend to be costly and are not used extensively for this reason. Scaling up of membrane technologies requires the materials and the fabrication process to

be economical. Polymers are used to prepare nanofiltration membranes due to ease of fabrication, flexibility, and low cost. Depending on the application, different polymers are used for nanofiltration, like PES, polyacrylonitrile, polysulfone, PVDF, polyimide, cellulose acetate, and polyamides [20]. Cellulose acetate and cellulose triacetate can be used to make NF membranes. The degradation of the cellulose based membranes can be prevented by using a masking agent like sodium hexametaphosphate [19].

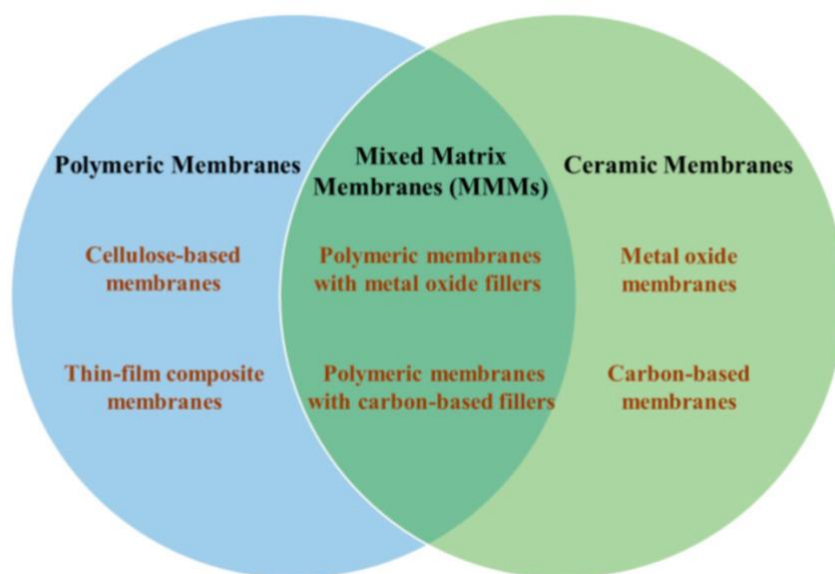


Figure 2.2: Materials that are commonly used to make nanofiltration membranes [19]. Adapted under the terms of the CC-BY 4.0 license. Copyright 2019, MDPI, Basel, Switzerland.

Recently, thin-film composite (TFC) NF membranes, made out of polymer, wherein two or more layers are combined to provide enhanced filtration activity are used for desalination processes. One such example of a TFC NF membrane is shown in Figure 2.3. In this figure, the top layer, which is termed as the ‘active layer’ is most commonly made of crosslinked polyamide. The second layer is the microporous substrate which can be made out of polysulfone, carboxylated

polysulfone, or PES . The backing layer is usually a thick non-woven polyester layer [21-23] . Besides the polymeric and the ceramic membranes, a third category of NF membranes exists, referred to as the mixed-matrix membranes (MMMs). These membranes are made by incorporating a metal oxide filler or an organic filler in a continuous polymeric phase [24, 25].

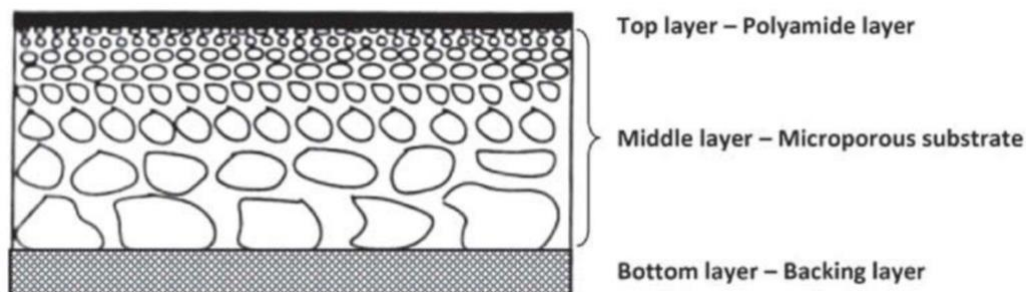


Figure 2.3: A schematic showing the different layers of a thin-film composite nanofiltration membrane [21] . Adapted under the terms of the CC-BY 4.0 license. Copyright 2014, Taylor and Francis.

PVDF is one of the membrane supports explored in this research. PVDF, a semi-crystalline thermoplastic (about 70% crystalline) [26], shows a low glass transition temperature of about -40 °C, and a melting point of about 180 °C [27]. The chemical structure of PVDF is shown in Figure 2.4. The fluorine in its backbone provides it with a high melting point along with chemical resistance. PVDF mainly exists in its α form, although its β form exhibits piezoelectric and ferroelectric properties, making it useful as a space application material as listed by NASA [28]. Besides NF membranes, PVDF finds applications in piezoelectric sensors, oil and gas industry pipelines, for 3D printing biomedical sensory devices, and as a composite with conductive fillers

for use in flexible electronics [27, 29-32]. For use in high temperatures, PVDF is often chemically crosslinked with other materials [33].

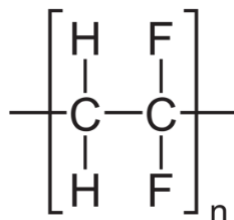


Figure 2.4: Structure of PVDF – Attribution - By NEUROtiker - Own work, Public Domain,

<https://commons.wikimedia.org/w/index.php?curid=3813386>

Aside from PVDF, PES was also used as a membrane support material in this research. PES is an amorphous thermoplastic, has a density between 1.2 to 1.8 g/cm³, and a glass transition temperature of about 225 °C. PES is particularly attractive for membrane filtration since it is resistant to chemicals like acids, alkalis, and hydrocarbons. The structure of the polymer is shown in Figure 2.5. The aromatic part of the polymer backbone provides thermal stability to PES, which coupled with its high stiffness and dimensional stability and a low flammability. These properties make PES useful for automotive applications like sound insulation and the hood of the car [34, 35], for hemodialysis membranes in the medical industry, for cell cultures to provide an environment for cell growth, and in microcapsules for drug delivery as well [36, 37]. PES has a hydrophobic surface, however, it can be made more hydrophilic by surface treatments, so as to introduce hydroxyl or carboxyl groups. Nevertheless, PES shows hydrogen bonding with water, making it more hydrophilic than PVDF.

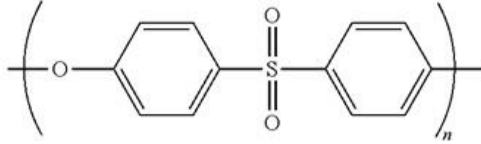


Figure 2.5: Structure of PES – Attribution –By Jü - Own work, CC0,

<https://commons.wikimedia.org/w/index.php?curid=19216919>

2.2. Reduced graphene oxide (rGO) used in separation membranes. Graphene, discovered by University of Manchester professors Giem and Novoselov [38], has attracted significant interest due to its unique structure and chemical characteristics. Graphene is essentially a 2D form of carbon [39], a single layer of carbon atoms arranged in a way to provide a high electron density to graphene. The most straightforward method to obtain graphene is to use a tape and exfoliate the top layer of graphite [40]. Graphene is resistant to chemicals and pristine graphene has a theoretical stiffness of 1 TPa [41, 42]. Pristine graphene shows electrical conductivity as high as 6×10^5 S/m, a high thermal conductivity of 4000 W/m-K [43, 44], and has a Seebeck coefficient of 350 μ V/K [45]. Graphene cannot be dispersed in water and organic solvents, and solvents like ethanol and dimethylsulfoxide (DMSO) are usually used to disperse graphene [46, 47]. When graphene is oxidized to graphene oxide (GO), it loses some of its electrical conductivity, but becomes dispersible in water due to the presence of polar groups. The structure of GO has been described by the famous Lerf–Klinowski model, wherein there are islands of aromatic rings in the structure of GO, which are separated by double bonds and functional groups like epoxy and hydroxyl [48, 49]. GO is reduced to reduced graphene oxide (rGO) since the latter has electrical properties and a structure closer to those of pristine graphene. However, rGO is not as dispersible in water as GO [50]. The stacking of rGO galleries, coupled with its chemical resistance and thermal stability,

makes rGO an attractive candidate for a variety of applications in the pharmaceutical industry, in the paper-making industry to filter kraft liquor, drinking water purification, natural gas purification, and for rejection of organics and inorganics [51-56]. The simplified structures of graphene, GO and rGO, and a basic understanding of how rGO is obtained from graphene, is shown in Figure 2.6.

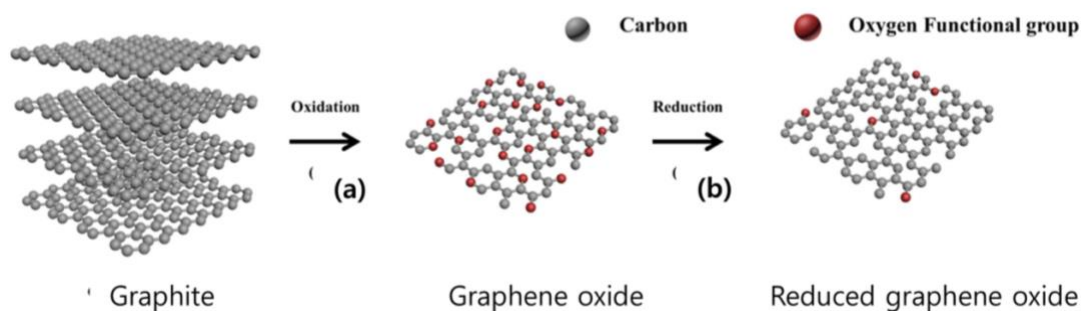


Figure 2.6: Schematic showing the structure of graphene, GO and rGO [57]. Adapted under the terms of the CC-BY 4.0 license. Copyright 2015, Korean Carbon Society.

The conversion of graphite to GO was done by Brodie in 1859 by adding potassium chlorate to graphite in fuming nitric acid. Another method was proposed wherein concentrated sulfuric acid was used along with nitric acid, and this approach was called the Staudenmaier method named after its founder [58]. However, to reduce the reliability on such highly concentrated acids, high temperatures involved in the Staudenmaier method, and the slow pace of the reaction, Hummers and Offeman introduced a new way of producing GO [59-61]. This method, which used sodium nitrate and potassium permanganate, dissolved in concentrated sulfuric acid, is today called the Hummers method (Figure 2.7). The use of KMnO_4 made the reaction faster, and there was no ClO_2 gas produced since no chlorate was used [62]. While this was a quick method to GO, the challenges

of the toxic gases produced (like NO_2 and N_2O_4) remained unresolved [59]. Most of the research done today uses some sort of modified version of the original Hummers method. Some of the modified methods include changes like getting rid of the NaNO_3 used in the process, pre-oxidizing graphite before adding KMnO_4 , partially replacing KMnO_4 with K_2FeO_4 , or reducing the amount of concentrated sulfuric acid used. The goal of the modifications to the Hummers method is to synthesize GO by reducing or removing the toxic gases produced, reducing costs and reaction time, improving scalability and making the whole process eco-friendly [59, 63-65].

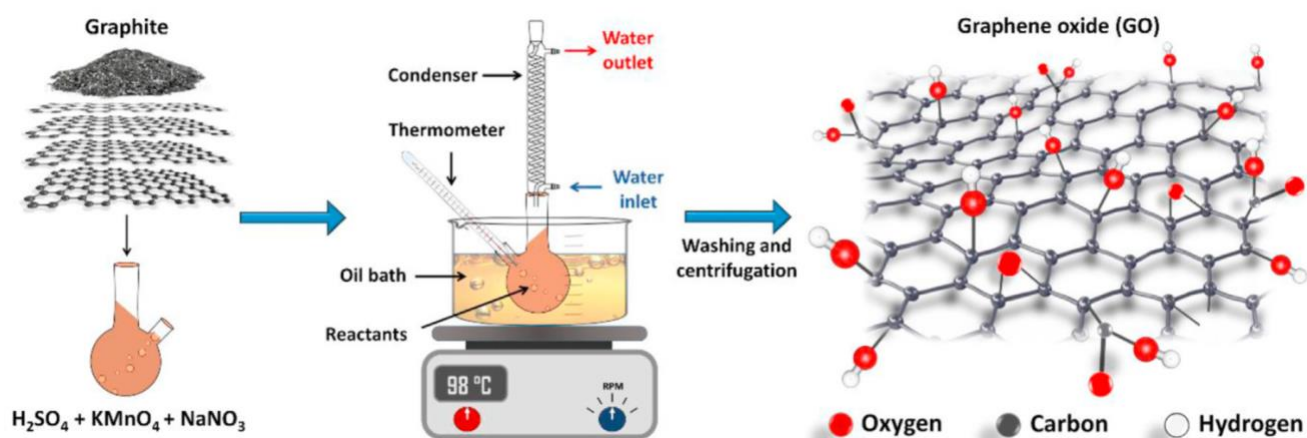


Figure 2.7: A schematic showing the Hummers method used to synthesize GO from graphene [62]. Adapted under the terms of the CC-BY 4.0 license. Copyright 2021, The Authors.

Published by Elsevier Ltd.

GO can be reduced to rGO using electrochemical reduction wherein the reducing agent is an electron [66]. rGO can also be obtained by thermal reduction of GO powder at a temperature between 200-400 °C. Thermal reduction is a low-cost method of obtaining rGO from GO [67, 68]. Another method to reduce GO is the hydrothermal method wherein only water along with nitrogen or hydrogen gas is required to reduce GO in an autoclave at a moderate temperature of 180 °C,

wherein a particular work in literature shows that applying a pressure of 40 bar helps drive the reduction process [69]. While hydrothermal reduction is an environmentally friendly option of reduction, using a biomolecule is also a green approach to reduce GO to rGO [70]. Some works have reported the use L-cysteine [71], which is an amino acid, to reduce GO to rGO. The chemical method to reduce GO involves different reducing agents like hydrazine hydrate, sodium hydroxide, or sodium borohydride [72, 73].

Efforts in the field of rGO membranes and films have been made by research groups exploring rGO nanofiltration membranes wherein rGO is intercalated with a polyelectrolyte for use in biological membranes and to fabricate rGO membranes for conductive electrodes [74, 75]. A group at University of Manchester has worked to develop rGO flexible barrier films which are inert to gases and water vapor, to be used in the medical and biological industries [76]. rGO can be intercalated with carbon nanotubes (CNTs) for drinking water purification, blended with titanium dioxide for water softening membranes, and can be used to make nanocomposites with metal oxide nanoparticles to make nanofiltration membranes [51, 77, 78]. While GO membranes have been explored in previous works from the Nair Group at Georgia Tech [79, 80], a shift to rGO was required to decrease the interlayer spacing and also to get better salt rejection results [56]. A particularly intriguing property of graphene (or GO or rGO) is the stacked structure that it exhibits [81], which provides a tortuous pathway to the incoming wastewater, allowing water to pass through while rejecting the unwanted solutes.

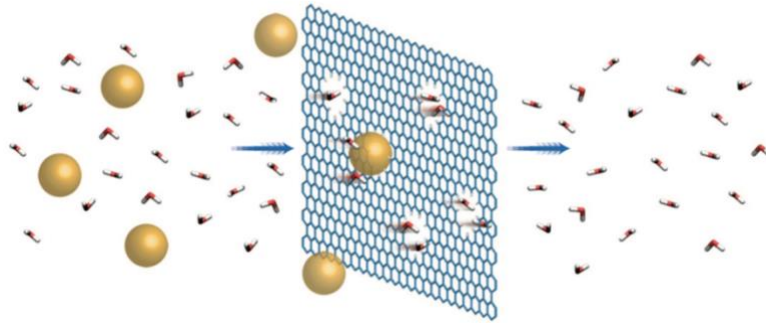


Figure 2.8: A schematic showing how a typical graphene membrane works (for RO). In this figure, the water molecules, indicated by red and white, pass through the membrane, whereas the larger golden particles which could be salt ions or other unwanted ions, are blocked. The blue arrows in the figure are indicative of the pressure which drives this filtration process [82].

Reprinted with permission. Copyright 2012, Springer Nature Limited.

Polymer-supported rGO shows a prominent substrate effect, wherein the mechanical properties of this composite-like system are dominated by those of the polymer support. To understand the properties of the rGO layer, FS films of rGO can be produced and characterized. These films have applications outside of membrane studies as well. Wearable electronics need to be smaller but flexible, and capacitor sizes need to decrease while electron transport needs to be optimized, lithium ion batteries require smaller cathodes – all these applications call for the fabrication of FS graphene or rGO films [83-85]. These films are analogous to bucky papers or FS carbon nanotube films [86]. Another application of the FS rGO films is in rejecting salts during the desalination process. A schematic showing the stacked rGO layers rejecting the salts and only allowing the water to pass through has been shown in Figure 2.9. Drawing inspiration from FS CNT papers, much research in literature has been directed towards developing FS graphene and GO. There are a number of ways to make FS GO films some of which include spontaneous delamination from a

polymer support like mixed cellulose ester (MCE) [85, 87], a method involving camphor and etching on copper [85, 88], self-assembly and solvent evaporation [85]. rGO does not have a very high electrical conductivity, and to overcome this challenge, there has been research to develop FS films of rGO which can be used for photoelectric devices [89-91].

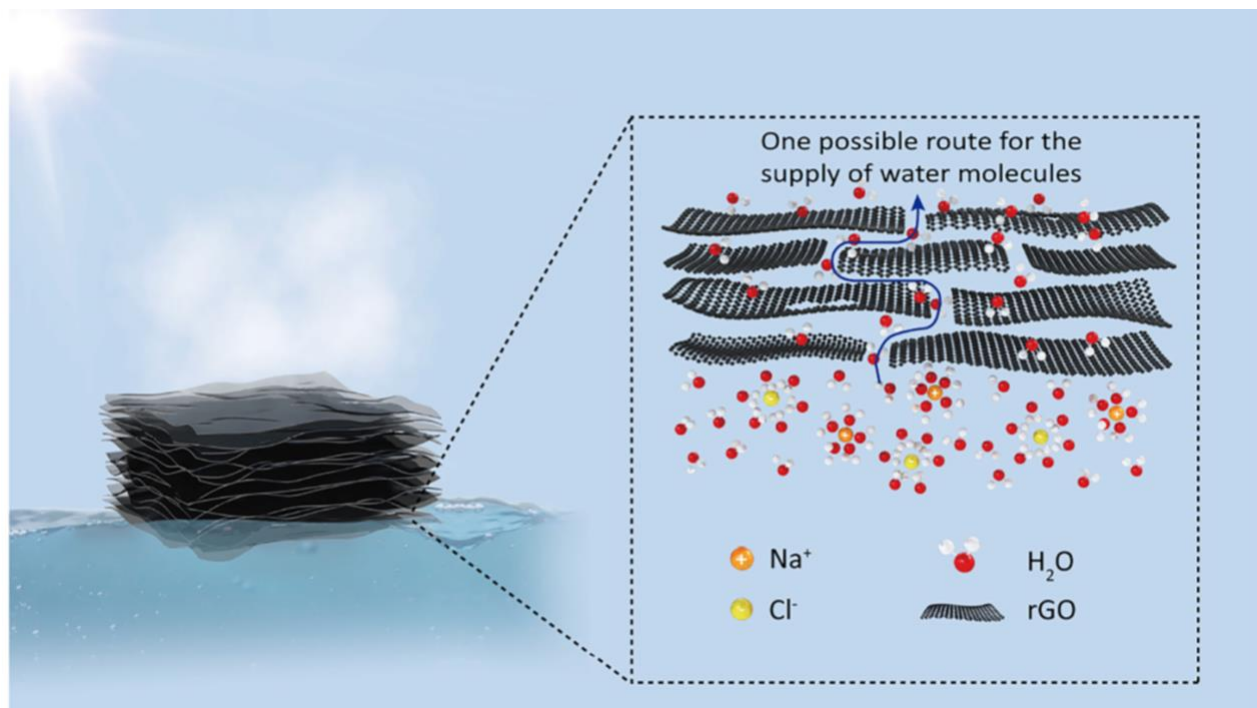


Figure 2.9: Stacked layers of free-standing rGO are capable of acting as membranes to reject the salts during the desalination process. In this research study, the water was evaporated using solar energy [92]. Adapted under the terms of the CC-BY 4.0 license. Copyright 2020, Pengyu Zhuang et al. Published by De Gruyter, Berlin/Boston.

2.3. Intercalants used for separation membranes. Intercalants are molecules which can be added in a structure to play a functional role in some process. To funnel down this definition, pertaining to this project, an intercalant improves the rejection properties of the nanofiltration membranes

and thereby the overall performance of the membranes. Intercalants can come in various forms like nano-alumina, methyl phosphonic acid, ferric oxide, or phytic acid which is derived from plant seeds. Ions, like K^+ , Na^+ , Li^+ , Mg^{2+} , and Al^{3+} , can also act as intercalants in separation membranes, depending on the composition and application of the membranes [93]. The choice of the intercalant is largely governed by the chemical interactions of the intercalant and the other components, the cost of the intercalant, and the ease of formulation and scale-up [94]. While intercalants increase the d-spacing inside the membrane microstructure, these molecules or ions have shown an increase in the rejection numbers for the membranes as well. The intercalants provide hindrance or act as a barrier as the solute tries to pass through the membrane, thereby increasing rejection. MXenes and GO membranes are often intercalated with molecules or ions of different shapes, sizes and forms. In literature, GO membranes have been fabricated with multifarious intercalants like titanium dioxide, silicon nitride, boron nitride, silicon dioxide, surfactant like cetyltrimethylammonium bromide (CTAB), carbon nanotubes, and dye molecules like acid orange, methyl blue, crystal violet, chrome black, Congo red, and eosin [93-97]. These intercalants are also called ‘nano spacers’ in literature [94], since their primary function is to tune or modify the interlayer spacings in the membrane. Figure 2.10 shows a polyamide membrane having a GO layer which incorporates nanoparticles like titanium dioxide, silicon nitride, and silica as intercalants. The tortuosity provided to the incoming water and the sieving of the ions/molecules can be seen in this schematic [96]. In that work, the intercalated membranes were able to reject organic dyes like methylene blue, basic fuscine, methyl orange and Evans blue from industrial wastewater while maintaining a flux between $11-15 \text{ Lm}^{-2}\text{hr}^{-1}\text{bar}^{-1}$ depending on the intercalant chosen between TiO_2 , SiO_2 , and Si_3N_4 . After incorporating TiO_2 as the intercalant, the interlayer spacing increased from 0.753 nm to 0.798 nm, and this increase led to an increase in water flux, while the intercalant molecules continued to reject the dyes satisfactorily by providing physical size sieving.

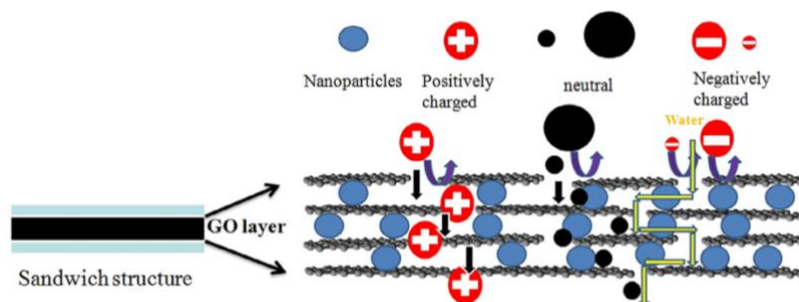


Figure 2.10: A schematic showing the sieving effect and the tortuosity to the path of incoming water provided by the intercalated GO-polyamide membrane. The intercalants are shown as blue nanoparticles in this figure [96]. Reprinted with permission. Copyright 2018, Elsevier.

2.4. Bridging the gap in literature. In conclusion, polymers are attractive support materials for NF membranes owing to their ease of fabrication and low cost. This research specifically describes the use of PVDF and PES polymers as support materials, having a thin layer of rGO on top (Figure 2.11 shows the schematic for the membrane). rGO is suitable for treating industry wastewater since it is chemically resistant and mechanically robust. Moreover, the stacked layers of rGO provide a sieving effect, and reject the unwanted molecules, allowing only water to pass through. The intercalants (different dye molecules in this case), act as hindrances in the galleries of rGO, further improving the rejection properties of the membranes. There are different works in literature which describe the use of polymer-supported GO/rGO membranes, the use of intercalants, FS GO films, and the application of micromechanical models to composite systems. This project aims to cover these different areas of research, for a family of membranes, by providing results obtained from a comprehensive set of mechanical tests. The findings of this research aim to support the further development of these membranes and an understanding of their performance, by investigating the effects of different polymer supports and intercalants on the processing-structure-property

relationships of rGO membranes. While there has been research on FS films in literature, this project details not only the fabrication and imaging but also the axial and transverse mechanical properties of the FS rGO/rGO-X films. Based on the initial dataset collected, these results will assist in the future design of similar membranes, enabling the production of a family of rGO-based membranes with specific performance targets. Figure 2.11 shows schematically the rGO/rGO-X on polymer membrane used in this research. The rGO/rGO-X layer was approximately 130 nm thick, whereas the polymer support was significantly thicker.

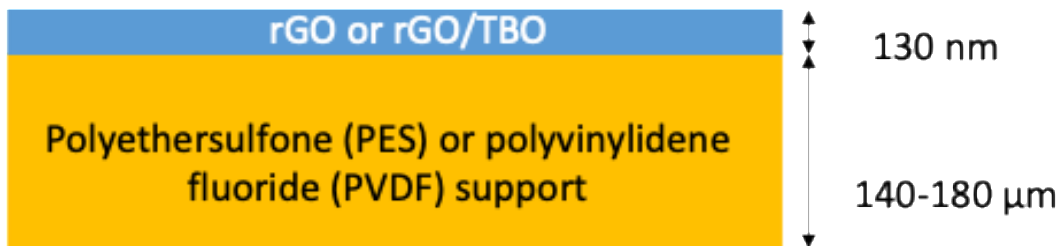


Figure 2.11. Schematic of the polymer-supported rGO/rGO-X membrane used in this research

CHAPTER 3: MATERIALS AND METHODS

The primary focus of this project was to quantify and compare the mechanical properties of rGO/rGO-X polymer membranes as well as assess the effects of processing conditions such as compaction and water addition on the mechanical properties of the membranes. For this purpose, different testing methods such as tensile testing, nanoindentation, and fragmentation were employed. To understand the microstructure of the membranes, scanning electron microscopy (SEM) was used. Furthermore, to isolate the effects of the rGO/rGO-X layer from the underlying support, FS rGO/rGO-X films were synthesized and tested. This chapter discusses the general theory for the tests and how they helped in the study. Following the testing theory, materials and sample preparation is discussed. The last part of the chapter touches upon the test methodology specific to the project.

3.1. Materials:

PES Ultrafiltration (UF) membranes and PVDF TriSep Flat Sheet UB70 UF membranes (manufacturer – Mann+Hummel Water and Fluids Incorporation) were purchased in roll form, from Sterlitech Corporation. Both membranes had an effective pore size of 30 nm, and the PVDF membrane had a nonwoven polyester backing material. The MCE membrane filters were purchased from Millipore Sigma and had a diameter of 90 mm and a pore size of 25 nm. The GO suspension was made using the modified Hummers method as has been described in previous work from the Nair Group [80], and the GO was reduced to rGO using NaOH. The concentration of the GO suspension was 1 g/L. Different dye molecules, referred to as intercalants, were added to the rGO suspension. The intercalants, toluidine blue O (TBO or TZ-1), methylene blue (TZ-2),

methylene green (TZ-3), thionin (TZ-4), bismarck brown (AZ-1), allura red (AZ-3), crystal violet (TM-1), galloxyanin (OX-1), and eosin-b (FL-1), were purchased from Sigma Aldrich.

3.2. Sample Preparation:

The samples tested as a part of this thesis included membranes supported on two polymers, PES and PVDF. The membranes were tested under different conditions, i.e. the dry and wet states along with the as-produced and compacted states, to understand the effect of processing conditions on the mechanical properties of the membranes.

The mechanical testing, production and characterization of FS films, and modeling work described in this thesis were a part of a larger project that was aiming to produce membranes and characterize their performance in selected feed streams. The sample preparation was performed by other team members on this project, but a brief overview of the sample preparation is provided here for reference. To begin the membrane production process, a GO suspension was prepared by the modified Hummers method, followed by the reduction of GO to rGO by NaOH. The intercalants were added into the rGO suspension as a drop-wise additive at different weight loadings, and these suspensions were used to prepare the membranes. The rGO suspension was sonicated with the desired amount of 0.5 g/L of the dye solution for 5 minutes before vacuum filtering this suspension on the polymer membrane. The rGO-TBO dispersions were made using 0.05 mg, 0.1 mg, 0.25 mg and 0.5 mg of TBO, per mg of rGO, for the PVDF supported membranes. The rGO-X dispersions had mass ratio 10:1 for the other intercalants supported on PES.

3.2.1. Preparation of bare polymer supports (PES and PVDF), rGO-polymer membranes, rGO-X-polymer membranes, and their compacted counterparts:

A piece of the PES or PVDF support was cut from the roll and then a circular sample of 90 mm diameter cut from this piece. The supports were kept in a sealed bag to maintain the slightly wet state of the membranes. The roll direction was marked while preparing the samples since the uniaxial tensile tests were conducted parallel to the roll direction. The rGO/rGO-X suspension was vacuum filtered on the porous polymer support (PES or PVDF), followed by drying and/or hydraulic compaction. Table 3.1 shows the different membranes tested in as a part of this research.

Table 3.1: List of membranes used in this work

Membrane	State	Intercalant	Loading(s) of the intercalant (wt.%)
Bare PVDF	Dry non-compacted	-	-
Bare PVDF	Dry compacted (compacted using the crossflow cell at 30 bar and the hydraulic press at 30 bar)	-	-
Bare PVDF	Wet non-compacted	-	-
Bare PVDF	Wet compacted (compacted using the hydraulic press at 30 bar)	-	-

Table 3.1 Continued

rGO-X on PVDF	Dry non-compacted	TBO/TZ-1	0, 4.8, 9.1, 20, 26
rGO-X on PVDF	Dry compacted (compacted using the dead-end cell at 30 bar)	TBO/TZ-1	0, 4.8, 9.1, 20, 26
rGO-X on PVDF	Wet non-compacted	TBO/TZ-1	0, 4.8, 9.1, 20, 26
rGO-X on PVDF	Wet compacted (compacted using the dead-end cell at 30 bar)	TBO/TZ-1	0, 4.8, 9.1, 20, 26
Bare PES	Dry non-compacted	-	-
Bare PES	Dry compacted (compacted using the hydraulic press at 30 bar)	-	-
rGO-X on PES	Dry non-compacted	TBO/TZ-1	0, 9.1, 26
rGO-X on PES	Dry compacted (compacted using the dead-end cell at 30 bar)	TBO/TZ-1	0, 9.1, 26
Bare PES	Dry compacted (compacted using the hydraulic press at 50 bar)	-	-
rGO-X on PES	Dry non-compacted	TZ-1, TZ-2, TZ-3, TZ-4, AZ-1, AZ-3, TM-1, OX-1, FL-1	0, 9.1

Table 3.1 Continued

rGO-X on PES	Dry compacted (compactd using the dead-end cell at 50 bar)	TZ-1, TZ-2, TZ-3, TZ-4, AZ-1, AZ-3, TM-1, OX-1, FL-1	0, 9.1
--------------	--	--	--------

The vacuum filtration, which took 5-10 minutes to complete, used a Rocker 300 or a Rocker 400 vacuum pump. After vacuum filtration and 24 hours of drying at room temperature, a circular shape of nominal diameter of 47 mm was cut from the larger 90 mm diameter membrane and then were supported by a ceramic holder and placed at the bottom of the HP4750X Sterlitech dead-end stirred permeation cell. For compacting the rGO-polymer membranes, hydraulic pressure was applied using ultrahigh purity nitrogen gas. The maximum capacity of this high-pressure cell was 300 ml, with a maximum pressure of 2500 psi (~172 bar). A transmembrane pressure (TMP) of 30 bar was used for 48 hours for PVDF based membranes, and a pressure of either 30 bar or 50 bar was used for PES based membranes, depending on the purpose of the experiment. The rGO-TBO on PES membranes were compacted at 30 bar to compare the tensile testing and the nanoindentation results obtained from the change in substrate. The rGO-X on PES membranes were compacted at 50 bar, since this TMP would be used for the flux and permeation measurements on these membranes (this will be related to a part of the upcoming paper from the Nair group at Georgia Tech). As a part of the component effect studies involving different intercalants, a PES supported membrane containing the baseline intercalant TBO, was also compacted at 50 bar. To simulate these compaction conditions for the bare polymer supports (PES and PVDF), the supports were compacted using a hydraulic press (Carver model 4386) for a period of 48 hours. The compaction was performed by holding the supports under a pressure of 30 or 50 bar during the day and 10 bar pressure overnight over a span of 48 hours. A simulated compaction procedure for the bare supports was used because the water flux through the bare supports was

high in the dead-end cell, making it impractical to compact the supports in the same way as the rGO and the rGO-X membranes. The data for the PVDF supports compacted by the hydraulic press was used for the nanoindentation experiments of the dry membranes, and for the tensile and nanoindentation tests of the wet membranes. However, for testing the dry PVDF support in tension, PVDF was compacted using crossflow conditions. The TMP was maintained at 30 bar during the day and 10 bar overnight for a span of 48 hours, using the crossflow module set-up (Pioneer CF047) which had a volumetric flow rate of 0.01 gallons per minute. The crossflow compaction was done so as to simulate the membrane processing conditions as closely as possible for the PVDF support. Figure 3.1 schematically shows the steps involved in the membrane fabrication process.



Figure 3.1: Steps involved in the fabrication of the membranes.

The membranes containing intercalants were prepared in a similar fashion as the membranes with only rGO. The 0.5 g/L intercalant solution was prepared by adding 0.5 g of the dye in 1L of DI water. The intercalant was used as a drop-in additive, and the rGO suspension was sonicated with the desired amount of this dye solution for 5 minutes before vacuum filtering this suspension on the polymer membrane. The same vacuum filtration process was followed to fabricate the membranes as was used with TBO [98].

The following calculation for a 3.5 in x 4 in sample shows how the equivalent pressure was determined for compacting the supports using the hydraulic press:

1. Convert bar to Pa (N/m²): 50 bars = 5×10^6 N/m²
2. Convert N/m² to N by multiplying by sample area: 5×10^6 N/m² x 0.00903224 m² = 45161 N
3. Divide by gravity: 45161 N / 9.81 m/s² = 4604 kg
4. Divide by 1000 to get metric tons from kg: 4604 kg / 1000 kg/metric ton = 4.6 metric tons.

Note: if other dimensions are used, multiply by 5×10^6 N by the total area in m² of the sample that will be compacted.

The rGO-TBO dispersions had mass ratios of 1:1, 2:1, 4:1, 10:1 and 20:1 for the PVDF supported membranes, and a mass ratio of 2:1 and 10:1 for the PES supported membranes. The rGO-X dispersions had mass ratios of 2:1 for all other intercalants used in this study. The nominal loadings of intercalants used in this study were given by the following formula [80]:

$$\text{Amount of intercalant (wt.\%)} = \frac{\text{Amount of intercalant}}{\text{Amount of rGO} + \text{Amount of intercalant}} \times 100\%$$

The mass ratios of rGO-TBO dispersions corresponding to 20:1, 10:1, 4:1, and 2:1 is 4.8 wt.%, 9.1 wt.%, 20 wt.%, 26 wt.% respectively. The 10:1 mass ratio for the other intercalants corresponded to a 9.1 wt.% loading of those intercalants.

3.2.2. Preparation of wet membranes.

The membranes are being developed to filter industrial wastewater and hence exposure to water is one of the important conditions whose influence on the mechanical properties of the membranes needs to be studied. To study the effect of water on the axial and transverse mechanical properties of the membranes, the membranes were soaked in DI water in a sealed vial for 24 hours. The samples were then taken out of the water with tweezers and dabbed twice on each side on a weighing paper to remove excess water prior to testing. Soaking experiments were conducted for 24-, 48- and 72-hour long periods, but the water uptake by the membranes plateaued after a period of 24 hours, as was observed by weighing the membranes in the dry state initially, and then comparing the weight of the membrane in the wet state to the initial weight.

Only the PVDF based membranes were tested in the wet state. The samples with PES as the support polymer were not tested in the wet state since the rGO or the rGO-TBO layer was observed to delaminate from the underlying PES support when the sample was soaked in water.

3.2.3. Sample preparation for mechanical testing. Samples of the rGO and rGO-X membranes installed on polymer supports were cut from circular membranes for mechanical testing with tensile testing and nanoindentation. Strips of constant width (~6 mm) were cut from the circular membrane using the gage section of an ASTM D638 type II die. The samples were oriented so that the machine direction of the support material was parallel to the length of the strip. All the samples were cut into 6-7 strips and samples from the same location of the circular sample were used for the same test.

3.2.4. Preparation of the free-standing rGO/rGO-X films:

The FS films were prepared by vacuum filtration of the rGO/rGO-X suspension onto the 47 mm diameter MCE membrane filter. The vacuum filtration set-ups used to make the FS rGO/rGO-X films were purchased from Southern Labware, and each of these included a 47 mm glass vacuum filter holder with a fritted glass support base and a filtering flask kit. The vacuum filtration was carried out using a Rocker 400 vacuum pump which provided a vacuum pressure of 100 mbar. For each of the films, 32 or 50 ml of 1 g/L rGO suspension was diluted to 250 ml using DI water. The 32 ml suspension would give a film which would have 32 times the amount of rGO as that on the membrane (referred to as 32FS), whereas the 50 ml suspension would give an FS film which would have 50 times the amount of rGO as that on the membrane (referred to as 50FS). The vacuum filtration took 2-4 days to reach completion upon which the rGO/rGO-X-MCE membrane was dried in the oven at 35 °C for 24 hours. Then, the rGO/rGO-X-MCE membrane was soaked in DI water, with the rGO/rGO-X side facing up. Due to the hydrophilic nature of MCE, the rGO layer spontaneously delaminated from the underlying MCE in a few seconds, as is shown in Figure 3.2. The FS film was dried in the oven at 35 °C for 24 hours.

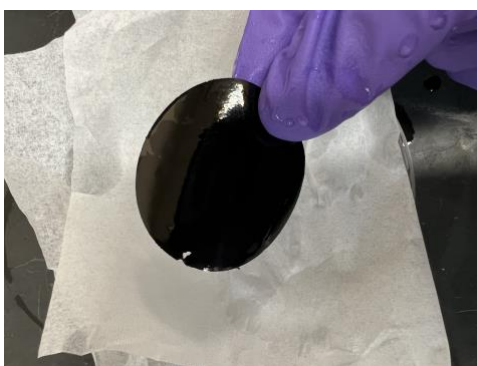


Figure 3.2: Image of a 50FS rGO film. The 50FS rGO film was stable to be handled manually.

After a couple of trial-and-error experiments, the precise experimental conditions were established. The vacuum filtration was done using a Rocker 400 vacuum pump which pulled a vacuum of 100 mbar (or 700 mm of Hg). The volume of DI water added to the rGO suspension was between 200-250 ml, and the DI water and rGO suspension were sonicated for 5 minutes. After the addition of the intercalant, the dispersion was again sonicated for 5 minutes. The vacuum filtration set-up is shown in Figure 3.3.

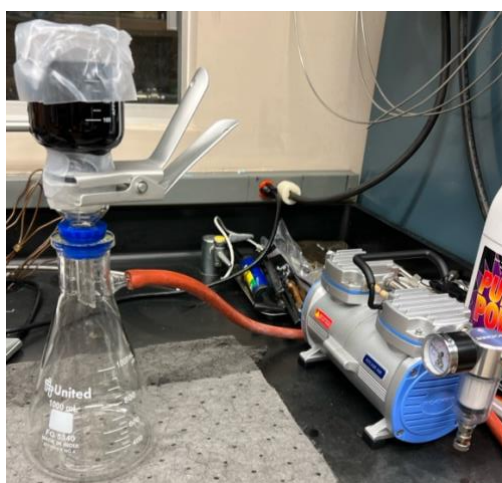


Figure 3.3: Vacuum filtration set-up used to make the FS rGO/rGO-X films.

3.3. Measurement Principles and Methods

3.3.1. Scanning Electron Microscopy (SEM)

Scanning electron microscopy (SEM) is a technique used for obtaining images of the surface and the cross-section of materials. It uses a ‘gun’ to eject electrons that are used to ‘scan’ or ‘image’ the surface of the sample. SEM gives a higher resolution than optical microscopy because of the lower wavelength or the higher energy of electrons that the former technique employs. SEM

imaging is mainly done by detecting secondary electrons and backscattered electrons. For non-conductive samples, the surface is usually gold sputtered so as to facilitate the imaging.

SEM was used to understand the microstructure of the porous polymers, along with the stacking of the rGO layers. Cross-sectional SEM was used to find the thickness of the rGO/rGO-TBO layer on PVDF, when different weight loadings of TBO were used. The same technique was also used to find the thickness of the rGO/rGO-X layer on PES.

SEM images, using a Hitachi SU8010 Cold Field Emission SEM, were collected for the bare polymer supports and the supported membranes. The membranes were cooled with liquid N₂, cut using tweezers, and were sputter coated with gold for 45 seconds using the Quorum Q-150T ES sputter coater. The FS rGO/rGO-X films were cut simply using tweezers and were imaged without any need for sputter coating.

3.3.2. Tensile Testing

The axial mechanical properties of the bare supports and the supported membranes were determined using tensile testing with a static load frame (Instron model numbers 68TMR44/55/5866 and 5566). The tests were conducted using an extension rate of 1.3 mm/min and a 100 N load cell. The strain was calculated using the original sample length of 22 mm, which corresponded to the grip separation at the start of the test. At least three samples were tested for each sample type. The thickness of the samples was measured using a thickness gauge (Neotek Digital thickness gauge, model TL342 NTK). Using the tensile testing data, values for modulus, tensile strength, and toughness were calculated. Tensile modulus was calculated from the toe corrected data over a strain range of 0.5 to 1.5%. The tensile strength was given as the maximum stress endured by the membrane before failure. The toughness was indicative of the energy

required to break the sample and was calculated as the area under the stress-strain curve [99]. The cross-sectional area used to calculate stress was based on the exterior width and thickness dimensions of the sample and did not account for porosity in the support material. Typical stress-strain curves for polymer films are shown in Figure 3.4. Since the instrument used for tensile testing underwent a retrofit service to update electronic components during the course of the research (as denoted by the two model numbers above), results obtained for the PVDF support before and after the retrofit service were compared to determine if the retrofit service affected the results. The force values at strain value of 0.01 mm/mm were not statistically different, so it was assumed that results obtained before and after the retrofit were comparable.

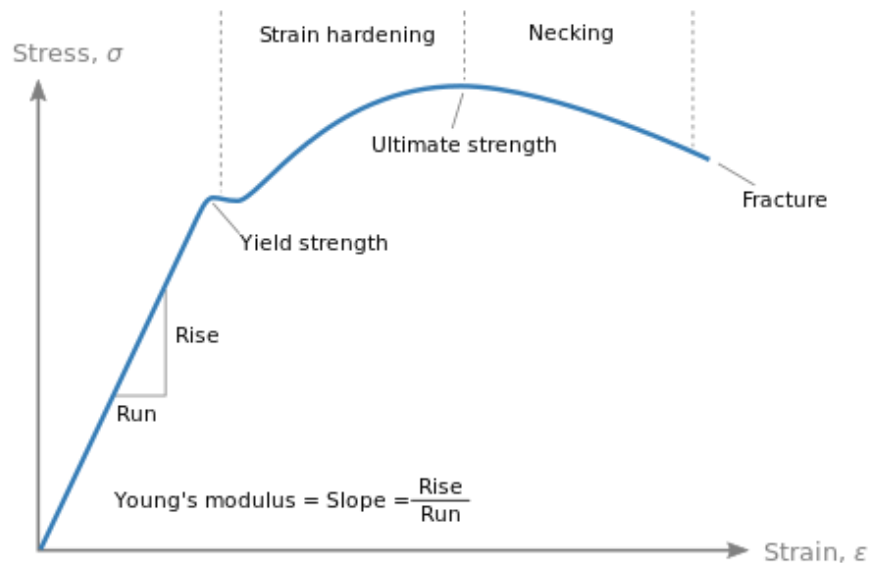


Figure 3.4: A typical stress-strain curve for a polymer film, showing the modulus, and the ultimate strength (or tensile strength). The area under this curve gives the toughness of the

sample. Attribution – By Nicoguardo - Own work, CC BY 4.0,

<https://commons.wikimedia.org/w/index.php?curid=89891144>

3.3.3. Nanoindentation and High-Speed Nanoindentation

Nanoindentation is typically used to measure the stiffness and hardness of thin film samples. The test comprises of an indenter of a specific geometry indenting into the sample, while the load displacement curve of the indenter is recorded by the instrument. This load-displacement curve helps calculate the stiffness and the hardness of the sample being indented. The indentation test consists of three segments, namely, the loading stage, the holding stage and the unloading stage. The stiffness in the transverse direction is denoted by the reduced modulus (E_r) and is associated with elastic deformation [100]. The Oliver-Pharr method [101] was used to calculate the E_r values, and the following equations were used to extract the E_r values from the load-displacement curve (1)

$$E_r = \frac{\sqrt{\pi}}{2\beta\sqrt{A_c}} S \quad (1)$$

Where A_c is the contact area and is expressed as follows:

$$A_c = C_0 h_0^2 + C_1 h_c + C_2 h_c^{1/2} + C_3 h_c^{1/4} + C_4 h_c^{1/8} + C_5 h_c^{1/16} \quad (2)$$

For the 1-micron radius cono-spherical indentation tip used in these measurements

Therefore, equation 2 can be expressed as:

$$A_c = -3.14h_c^2 + 6.28 \times 10^3 h_c \quad (3)$$

Where:

$$h_c = h_{\max} - \epsilon \frac{P_{\max}}{S} \quad (4)$$

In the above equations: β is the geometry correction factor equal to 1 since the indentation tip is spherical, ϵ is the intercept factor with a value of 0.75 [102], and S is the slope of the unloading curve. P_{\max} is the peak force value which is determined by the user. Now, equation (1) can be expressed as follows:

$$E_r = \frac{\sqrt{\pi}}{2 \sqrt{(3.14h_c + 6.28E_3h_c)}} \frac{\partial P}{\partial h} \quad (5)$$

Different load functions, customized for specific samples, can be designed by the user for nanoindentation testing (Figure 3.5). For this study, a trapezoidal load function was utilized, with a loading stage where the indenter tip presses into the sample (denoted by the red line). Once the designated load has reached the maximum value (P_{\max}), the indenter is held in position during the holding stage (denoted by the green line), ensuring proper stabilization of the indenter. Post the holding stage, the load function shows a decline to zero loading on the sample, indicative of the indenter moving out form the sample (denoted by the blue line).

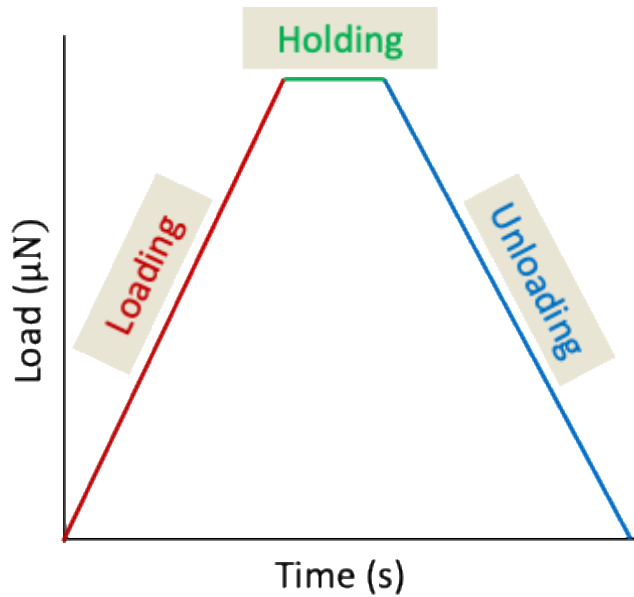


Figure 3.5: A typical loading-holding-unloading curve used in nanoindentation.

High Speed Nanoindentation (HSN) was used in this work as well. Commercially, high speed nanoindentation is referred to as Accelerated Property Mapping (XPM). HSN, introduced by the company Bruker, is a technique used to find the transverse stiffness of the samples, similar to nanoindentation, but 21 times as fast. This technique makes use of a grid and skips the piezo settlement and the drift measurements steps, thereby giving the results in a couple of minutes for 10 indentations, which would normally take half an hour by nanoindentation. HSN uses very fast electronic data acquisition and the loading, holding and unloading stages of the cycle are confined only to fractions of a second. This method is also referred to as ultra-fast nanoindentation [103, 104].

Nanoindentation experiments were performed using a nanoindenter (Bruker TI-980 Triboindenter). The sample strip cut from the as-produced circular membrane was mounted horizontally on a half-cylinder and held down by pins on both sides to ensure a stable surface for the indentation (Figure 3.6). The experiments were conducted using a conospherical diamond indenter with a $1.3\ \mu\text{m}$ radius and a maximum normal force of $40\ \mu\text{N}$. Ten indents were made on each sample, and a trapezoidal area function was used to calculate the values of reduced modulus (E_r). A box and whisker plot was constructed for each sample to identify and eliminate any outlier data points, and the average was taken thereafter using the remaining data points. The rGO-X/PES samples were examined with HSN using the same nanoindentation instrument. Given the difference in indentation rates, the values obtained by nanoindentation and HSN were not compared quantitatively.

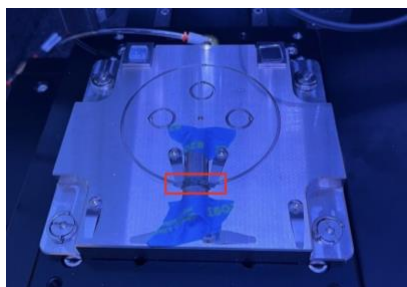


Figure 3.6: Experimental set-up for nanoindentation- the membrane sample (highlighted by the red box), is held down by pins onto a cylinder which is stuck on the stage.

The nanoindenter calculated the value of E_r using equation (1), where A_c is the contact area and β is the geometry correction factor of 1 since the tip is spherical. S is the slope of the unloading curve in the load-displacement curve for the indent and is representative of the sample stiffness. This expression for E_r accounts for the deformation in the indenter tip as well as the deformation in the

sample. However, the indenter tip which is made of diamond, is much harder than the sample, so the calculated value of E_r is assumed to be representative of the sample only.

HSN was used to measure the E_r values for the dry, PES supported membranes containing TBO and also the new intercalants. This technique was performed since the instrument was facing problems while performing nanoindentation at that time phase. However, since HSN was performed on all new intercalant containing membranes, this data set is self-comparable. The sample was mounted in the same way as shown for nanoindentation, and a trapezoidal load function was used for HSN as well. The indentation pattern and peak force values were kept the same as for nanoindentation, however, the loading, holding and the unloading times were modified. The loading and unloading times were set at 0.5 seconds, and the holding time was kept at 0.1 seconds. The data acquisition set was adjusted accordingly. A preload of 2 μN was maintained to ensure that the indenter was in contact with the sample surface.

3.3.4. Tensile testing of FS films

A small scale mechanical testing load frame (TA Instruments ElectroForce 3100 Mini) was used to test the FS rGO/rGO films. These films were brittle and required a small load cell to be tested in tension. A 1N load cell was used for testing these FS films at a shared facility (Biomechanics lab) in Georgia Tech. The extension rate was maintained at 0.008 mm/s for a gage length of 8 mm. This extension rate was chosen so that these tests would use a similar strain rate as the fragmentation testing of the supported samples. The clamps for the small-load tensile testing frame were manufactured using a 3D printer (Markforged Gen 2 21446), out of Onyx filament (a blend of nylon and carbon fibers), at the Montgomery Machining Hall at Georgia Tech. The clamps had

nylon screws (glass-filled nylon raised-head thumb screws, 1 high-strength, 10-32 thread size, 1” Long) for tightening and loosening purposes, which were purchased from McMaster Carr. The vinyl stickers used for mounting the free-standing films in the small-scale tensile testing load frame were obtained, and cut using the vinyl cutter Cricut Maker 3, at the Materials Innovation and Learning Laboratory (MILL) at Georgia Tech.

The 50FS films were chosen for this test over the 32FS films, since the former were stable when handled with tweezers and mounted in the tensile testing load frame. The width of the samples was kept below 2 mm to maintain a sample length to width ratio of 4:1. The width of the samples was measured using Image J software to get accurate values.

The small-scale tensile testing gave the load-displacement data of the FS films under tension. The fracture stress is the stress at fracture for the sample. This fracture stress value was calculated using equation (7):

$$\sigma_{frac} = \frac{\text{Load at fracture}}{\text{Cross sectional area}} \quad (6)$$

The modulus values were also calculated for the 50FS films. To do so, the stress and strain values were calculated for each of the film samples. The stress value at each point of the test was calculated by dividing the load (or the force) at that point by the cross-sectional area of the film. The elongation in the sample was found from the displacement data obtained from the test. The elongation, divided by the initial length of 8 mm, gave the strain values at each point of the test. The stress values of the samples were plotted against the strain values and the modulus was

calculated as the slope of the linear part of this curve. The reported modulus values are an average of the modulus values of two to three samples tested for each of the 50FS films.

3.3.5. Fragmentation Test

In addition to standard tensile testing to failure, tensile testing was used for fragmentation testing [105]. The adhesive strength value is indicative of how strongly the rGO is bound to the polymer support, and if the addition of an intercalant influenced this adhesion or not. Adhesion can vary substantially and affects the macroscopic mechanical properties even though the rGO-based layer is quite thin in comparison to the support thickness. In order to find the adhesive strength value, fragmentation testing was explored.

In fragmentation testing, the supported membrane samples were deformed in tension to a prescribed strain value which was 10%, that is, beyond the elastic limit but before sample failure. After being deformed, the sample was removed from the testing frame, and the sample surface with the membrane was imaged using an optical microscope (Keyence VHX 7000 series). The thickness of the rGO/rGO-X layer was found from the cross-sectional SEM images of the membranes. The fracture stress of the rGO/rGO-X layer was calculated using the small-scale tensile testing of FS rGO/rGO-X films. The testing produced cracks in the rGO/rGO-X membrane that propagated perpendicularly to the loading direction. Measurements of the crack spacing were made, and these measurements are used with the formula shown below to understand the interfacial adhesion in terms of the interfacial shear traction: (7)

$$\tau_{max} = \frac{3}{4} \pi \frac{h}{\lambda} \sigma_{frac}$$

where, τ_{\max} is the interfacial shear traction, h is the thickness of the rGO/rGO-X layer found from cross-sectional SEM images of the rGO/rGO-X on PES membranes, λ is the mean spacing between the cracks found by viewing the fragmented samples under the optical microscope, and σ_{frac} is the fracture stress of the rGO/rGO-X film which was calculated using the small-scale tensile testing of the FS rGO/rGO-X films.

A high value shear traction translates into a greater adhesion of the rGO/rGO-X layer on the porous polymer support. Fragmentation was used to quantify the interfacial shear traction between the rGO/rGO-X layer and the polymer support. For this, the samples were cut into strips similar to those for tensile testing, with the strips for the fragmentation test being taken from the same location on the circular sample so as to ensure uniformity across all samples.

Figure 3.7 shows one of the samples which was fragmented and then imaged on the same day. The white vertical lines on the sample are the cracks generated as a result of the fragmentation test. A horizontal line (denoted in yellow) is drawn perpendicular to the cracks. The length of this line is divided by the (number of cracks – 1) to find the mean or average spacing between the cracks.

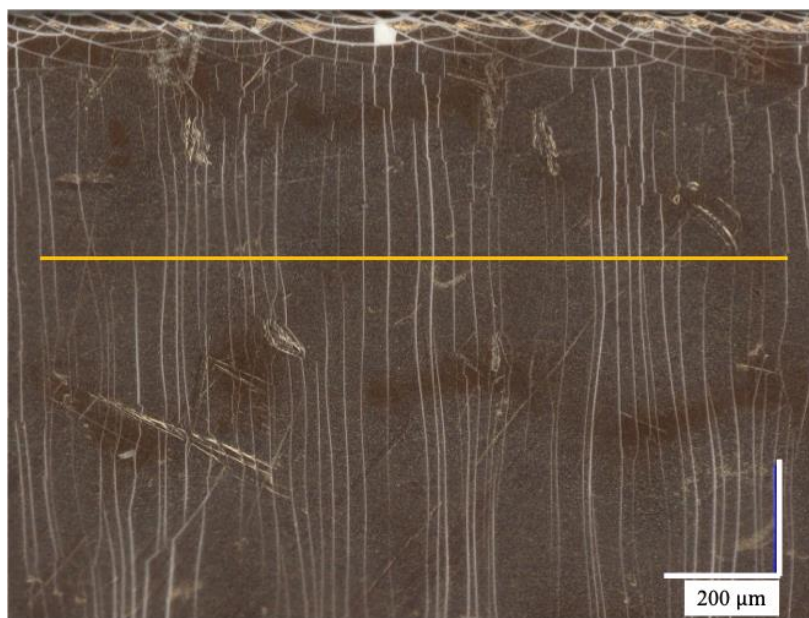


Figure 3.7: Fragmented compacted rGO-AZ-3 at a magnification of 200x.

A protocol (as shown in Figure 3.8) was set up for imaging the samples at multiple locations, and at three different magnifications of 200x, 500x, and 1000x. The fragmented membranes showed cracks throughout the length of the sample and not simply at two or three locations when viewed at these magnifications. The data used for the analysis were the edge-location data, that is, the cracks that originated at the edges of the fragmented membrane sample.

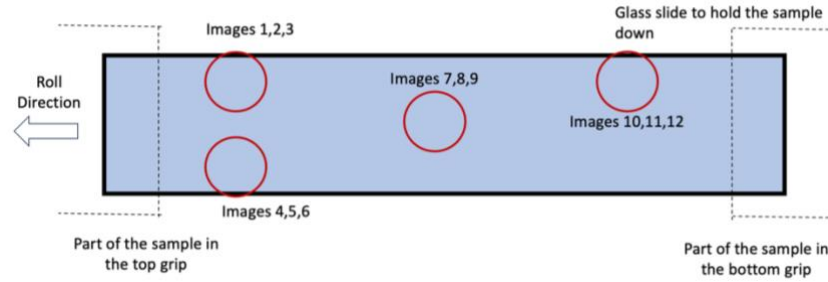


Figure 3.8: Protocol for choosing different locations on the fragmented sample to ensure that the cracks are observed at the edge and the central locations systematically

3.4. Modeling

In literature, micromechanical models like the inverse rule of mixtures or the lower bound mixing rule, have been used to quantify the mechanical strength of composites [106]. A modification of the inverse rule of mixtures is used for the transverse mechanical properties of the composites, known as the Bull Model [107]. This model focuses on the geometry of the indentation system and calculates the volume fraction as a function of the maximum indentation depth and the thickness of the coating layer. The mathematical form of the models and the expression for the volume fractions of the graphene and the polymer layers are shown in the equations below:

The inverse rule of mixtures or the lower bound rule of mixtures:

$$\frac{1}{E_C} = \frac{V_g}{E_g} + \frac{V_p}{E_p} \quad (8)$$

The Bull Model:

$$\frac{1}{E_c} = \frac{1 - a_B \left(\frac{t_f}{h}\right)}{E_g} + \frac{a_B \left(\frac{t_f}{h}\right)}{E_p} \quad (9)$$

$$a_B = \frac{\pi h \tan(\psi)}{\pi h \tan(\psi) + 2t_f} \quad (10)$$

Where E_c is the E_r value of the rGO/rGO-X layer supported on the PES polymer, E_p is the E_r value for the bare non-compacted PES support, E_g is the E_r value of the FS rGO/rGO-X film, V_g is the volume fraction of the rGO/rGO-X layer, V_p is the volume fraction of the PES support, t_f is the thickness of the rGO/rGO-X layer found from the cross-sectional SEM images of the rGO/rGO-X on PES membranes, h is the average h_{\max} (maximum indentation depth) value obtained from the nanoindentation experiment of rGO/rGO-X on PES sample, and ψ is the half angle of the tip conical indenter at the maximum load.

The volume fraction of the rGO/rGO-X layer was calculated by dividing the thickness of the rGO/rGO-X layer by the total indentation depth (h_{\max}) while indenting a supported sample. Subtracting this value from 1 gave the volume fraction of the polymer. These volume fraction values are not representative of the whole membrane sample, and only represent the volume of the sample which was indented. The E_g value was taken as the E_r value for the nanoindentation test performed on the lower side of the 50FS film. The lower side was the side in contact with the MCE membrane filter. The samples considered for the modeling were non-compacted rGO, rGO-TM-1, rGO-AZ-3 and rGO-TZ-1, on PES.

CHAPTER 4. EFFECT OF COMPACTION AND WATER ON THE MECAHNICAL PROPERTIES OF PVDF SUPPORTED MEMBRANES

The membranes were compacted using the dead-end permeation cell as a part of the membrane fabrication process. Moreover, the chief application of the membranes was to filter out wastewater, meaning that the membranes would be exposed to water. Given this information, hydraulic compaction and exposure of water could influence the mechanical properties of the membranes. This chapter aims to understand the effect that the compaction process and the introduction of water would have on the mechanical properties of the PVDF supported membranes. The axial mechanical properties of the membranes were tested using tensile testing, whereas nanoindentation was used to measure the transverse mechanical properties of the membranes. The baseline intercalant, TBO, was added at four different weight loadings in the PVDF supported membranes. The rGO/rGO-TBO membranes were compacted under a hydraulic pressure of 30 bar for a period of 48 hours and the bare PVDF membranes were compacted using the hydraulic press. The details of the compaction process, and the process to make wet membranes, has been described in the previous chapter.

As stated previously, multiple competing effects are at play which affect the mechanical behavior of these membranes: TBO loading and arrangement of the TBO molecules, pressure applied during membrane processing (compaction), locking/pinning of the rGO galleries by TBO, and the introduction of water for the wet membranes. To assess these effects, mechanical testing was performed on the membranes in four states: dry non-compacted, dry compacted, wet non-compacted, and wet compacted. In each of these four states, membranes containing different

amounts of TBO were tested to establish the processing structure-property relationships for these membranes. Additionally, the supports were tested using the same procedures and in similar states.

Typical stress-strain curves for some samples are shown below in Figure 4.1 for the dry compacted PVDF membrane samples. Each of the curves can be divided into two parts depending on the shape of the curve - the initial linear part of these curves shows the elastic deformation of the membranes, up to the yield stress, after which the membranes undergo plastic deformation as shown by the non-linear part of the curves. The maximum stress value that the membranes can withstand before failure is the tensile strength or the ultimate strength of the membranes, and the strain value at sample fracture is called the failure strain. The area under the curves gives the toughness or the energy absorbed by the membranes before failure. The curve shapes were similar for all samples wherein before failure, they experienced a recoverable elastic deformation up to the yield stress, followed by substantial plastic deformation. The failure strain was largely similar for the bare support and the supported rGO/rGO-X membranes.

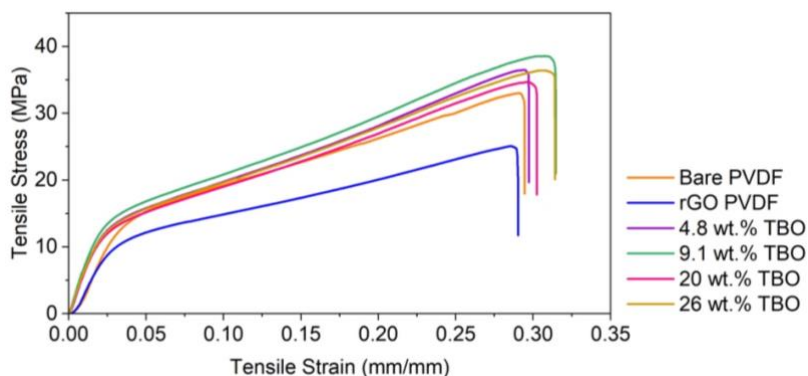


Figure 4.1: Representative stress-strain curve for the dry, compacted PVDF membranes.

Figure 4.2 depicts the properties obtained from tensile testing for the non-compacted and compacted dry rGO-TBO/PVDF membranes. The three properties calculated from this testing represent different types of responses. Modulus is associated with elastic (recoverable) deformation, while tensile strength and toughness are associated primarily with plastic (permanent) deformation. As described in the previous chapter, the cross-sectional areas used to determine stress values from tensile testing were calculated using the overall sample dimensions, which included void space in the porous support. This approach could overestimate mechanical reinforcement effects from compaction if compaction reduced the porosity in the support. To mitigate this effect, property changes for the rGO and rGO-TBO membranes are discussed relative to the bare support in the same condition. These results for the bare support are shown in Figure 4.2 as dashed lines representing the upper and lower bound measurement for each property. The compacted PVDF supports were prepared using a hydraulic press which was assumed to be a reasonable proxy for compaction in the dead-end cell.

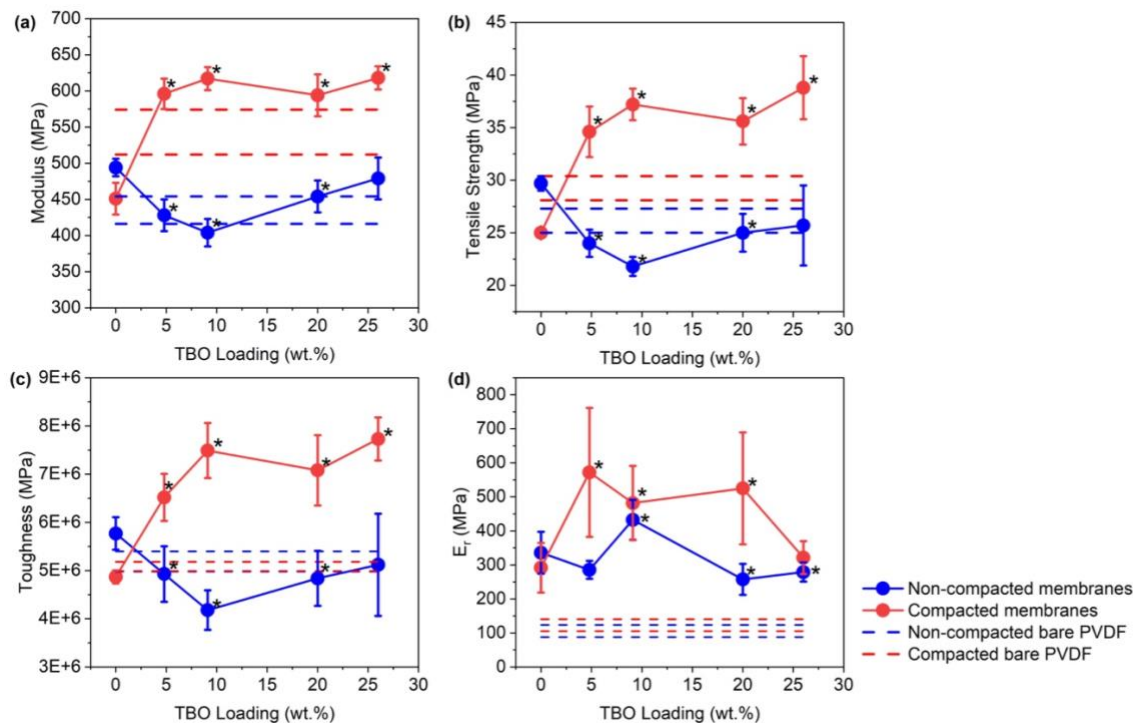


Figure 4.2: Modulus (a), tensile strength (b), toughness (c), and E_r (d) values for the non-compact and compacted PVDF membranes in the dry state. The asterisks (*) indicate statistically significant values when compared to the rGO-PVDF membranes using a t-test with a 95% confidence interval. The bare PVDF membrane has been shown with two dashed lines which represent the upper and lower bounds of the modulus value obtained from the standard deviation in that property.

For the non-compact membranes, the modulus values were similar to or slightly higher than the bare support. Also, the addition of TBO did not improve the modulus in the non-compact state. Considering the membranes with 4.8 wt.%, 9.1 wt.%, and 20 wt.% TBO and comparing these to the rGO membrane containing no TBO (Figure 4.2a), the tensile modulus decreased. At 20 wt.% TBO, the modulus began to increase, but it was not greater than that of the rGO membrane. The

modulus continued to increase for the membrane containing 26 wt.% TBO, and its value was similar to the rGO membrane. Since the membranes were prepared similarly, the change in modulus values was attributed to the TBO loading in the rGO layer.

Within the rGO galleries, TBO molecules could be arranged singly, i.e. isolated from other TBO molecules, or they could form clusters, which varied according to the number of molecules associated with them and their arrangement. As an example, a TBO dimer would include two molecules, and it could be arranged as an H-dimer (where the molecules are stacked vertically) or as a J-dimer (where the molecules are arranged laterally). Other arrangements are possible involving larger numbers of molecules (trimers, tetramers, etc.) and/or structures that are more disordered (termed I clusters). Work within the larger project conducted by Muskan Sonker examined how the molecules arranged as a function of the TBO concentration [98]. In that work, the population of TBO molecules existing as single molecules decreased as the TBO concentration increased. At a TBO concentration greater than 15 wt.%, the molecules showed a higher propensity to form clusters, with increases in both H-type and J-type clusters. This transition corresponded to the mechanical property changes observed in this work. The trend observed suggested that intercalated TBO in the form of single molecules disrupted van der Waals bonding between rGO layers but that intercalated clusters of TBO provided physical bonding that was able to compensate for modulus losses due to the incorporation of TBO, similar to z-pinning in laminated composites [108, 109]. Overall, the addition of TBO did not provide mechanical reinforcement in this range of TBO loadings. Additionally, tensile strength and toughness followed qualitatively similar trends to modulus as TBO loading increased.

The property results after compaction were different, and these results are also shown in Figure 4.2. Compaction was found to influence the properties of the bare support and the membranes. The

modulus, tensile strength, and toughness of the compacted support were increased relative to the as-received, non-compacted support material, and unlike the non-compacted membranes, the compacted membranes containing TBO showed higher modulus values than the bare support. With a TBO loading between 4.8 wt.% and 26 wt.%, the modulus increased relative to the rGO membrane, though the modulus was similar at all TBO loadings. Since the compacted membrane containing only rGO did not have a higher modulus value than the compacted support or the non-compacted rGO membrane, mechanical property increases in the compacted rGO-TBO membranes were associated with changes in the microstructure of intercalated membranes and increased adhesion between the components, which would include adhesion between layers in the rGO-TBO membrane and adhesion between the rGO-TBO membrane and the PVDF support.

In addition to properties associated with tensile deformation, the transverse modulus values of the supported membranes and the bare support were measured with nanoindentation and reported as the reduced modulus, E_r . The E_r values captured a more localized understanding of the membrane microstructure whereas the values from the tensile test provided a more macroscopic view. At the controlled force of 40 μN used in these tests, indentation depths varied from about 100 nm to approximately 650 nm across all samples, which included samples in the non-compacted and compacted states. These indentation depths were similar to or exceeded the thickness of the rGO-based layer, meaning that the value of E_r represented the rGO/rGO-TBO layer and the support and not just the rGO/rGO-TBO layer. However, the properties of the support did not dominate the results. The indentation depth was greater for the bare PVDF support in all conditions as compared to the membranes with the rGO/rGO-TBO layer, indicating that the E_r values of the rGO-based layer were higher than the bare support as expected.

Examining the results for the non-compacted membranes, the TBO concentration and resulting cluster structure had a different effect on the transverse modulus than the tensile modulus. In tension, the membrane structure was resisting sliding between rGO layers, whereas during indentation, the membrane structure was resisting flexure of rGO layers. When TBO existed primarily as single molecules between adjacent rGO platelets, the value of E_r was similar to that of rGO (4.8 wt.% TBO) or increased (9.1 wt.% TBO). As the TBO concentration increased and the arrangement of TBO transitioned from single molecules to clusters, the value of E_r decreased and then increased at the highest loading used in this work. In tensile tests of non-compacted membranes, membranes containing predominantly isolated TBO molecules had decreased values of modulus. However, in indentation tests, inclusion of single molecule TBO was able to reinforce the membrane, which was consistent with the type of deformation imposed. As the TBO concentration increased from 4.8 to 9.1 wt.%, the number of TBO molecules was sufficient to fill enough of the space between rGO platelets to provide resistance to indentation. When TBO concentration was increased further, the number of TBO clusters increased. Vertically stacked clusters would increase the distance between rGO platelets leading to less resistance to indentation when the spacing between TBO clusters was large and more resistance when their spacing was smaller, which was the result seen in this work.

Compaction also affected the modulus obtained from nanoindentation tests differently than the modulus from tensile testing. Compaction did not uniformly increase the values of E_r for the membranes containing TBO. Instead, membranes containing 4.8 and 20 wt.% TBO showed increased values of E_r , and membranes containing 9.1 and 26 wt.% had similar values of E_r as compared to their non-compacted counterparts. The change in E_r would be consistent with the structural reorganization due to compaction. For membranes with 9.1 and 26 wt.% TBO, no

significant change in E_r was observed after compaction. We postulate that this similarity between the non-compacted and compacted membranes at these TBO loadings correlate to a lesser ability to undergo structural reorganization when compacted. At these TBO loadings, the membranes may have reached a critical concentration of TBO monomers (9.1 wt.%) and dimers (26 wt.%) and reorganization was hampered. Additionally, the value of E_r was not changed for the membrane containing rGO only, which was similar to the tensile testing results.

The bare PVDF support data for tensile testing came from testing the crossflow-compacted PVDF support. To simulate the conditions used for the membrane preparation as closely as possible, the support was compacted under crossflow conditions at a TMP of 30 bar for a period of 48 hours. Figure 4.3 shows the force-strain curves for the non-compacted and the crossflow compacted PVDF supports. In this figure, the force-strain curves for the non-compacted and the crossflow compacted supports do not show substantial differences, indicating that the higher modulus value was a result of the change in the cross-sectional area when the support was compacted. Specifically, the reduced thickness of the crossflow compacted support led to an increase in the modulus values of the compacted support as compared to the non-compacted support.

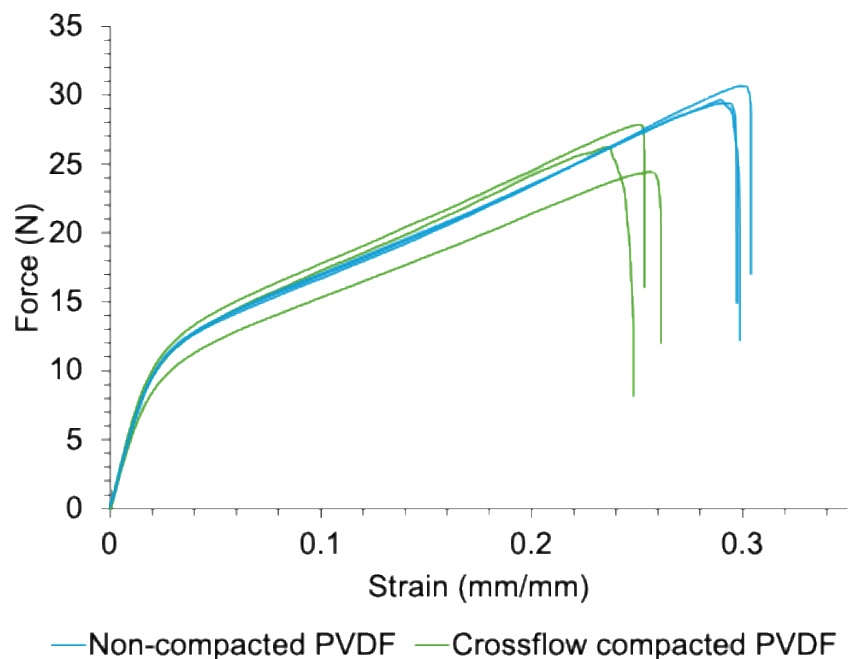


Figure 4.3: Force strain curves of the non-compacted PVDF support and the crossflow-compact PVDF support.

Figure 4.4 shows the axial and transverse mechanical properties of the wet membranes in the non-compacted and compacted states. The general trend in tensile modulus with TBO loading was similar to that seen for the dry non-compacted membranes, though the modulus values in some cases were lower than that for the bare support. For low TBO loadings of 4.8 wt.% and 9.1 wt.%, the modulus value decreased relative to the rGO membrane, whereas membranes with higher TBO loadings showed a modulus value similar to that of the rGO membrane. Similar results are seen for the wet compacted membranes in that values were lower than the bare support, indicating that including water in the structure negated the effects of compaction. The interactions between rGO and TBO could be reduced when water is present due to swelling of the rGO layers, leading to the layers sliding relative to each other when loaded in tension (parallel to the rGO platelets). Under

these conditions, the value of modulus would be reduced. The other axial mechanical properties, tensile strength and toughness, shown in the figure follow the trends shown by the modulus values of the wet samples.

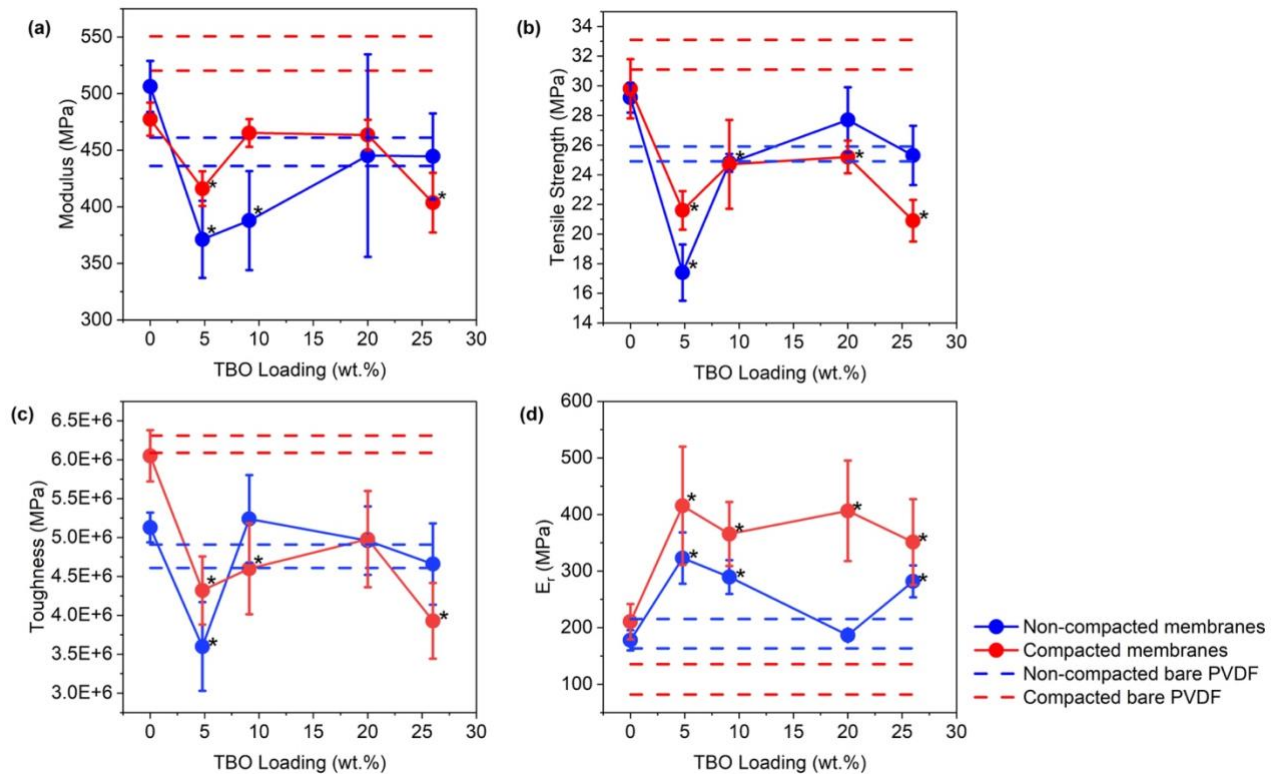


Figure 4.4: The modulus (a), tensile strength (b), toughness (c), and E_r (d) values for the wet PVDF supported membranes having different loadings of TBO. The asterisks (*) indicate statistically significant values when compared to the rGO-PVDF membranes using a t-test with a 95% confidence interval. The bare PVDF membrane has been shown with two dashed lines which represent the upper and lower bounds of the mechanical property obtained from the standard deviation in that property.

For the nanoindentation measurements of the wet non-compacted membranes, the behavior of the membranes containing 9.1 wt.% and 26 wt.% TBO was qualitatively similar to that of their dry counterparts. However, the membrane containing 4.8 wt.% TBO showed an increase in the E_r value relative to the rGO membrane in the wet state, which was not observed for the dry membranes. Compared to the membrane containing only rGO, the introduction of the TBO molecules, arranged as monomers at 4.8 wt.% loading, could be resisting the flexure of the rGO layers, by adding transverse stiffness to the membranes. The compacted wet membranes showed a similar trend in E_r values as their dry counterparts, at all loadings of TBO below 26 wt.%. At 26 wt.%, the membrane containing TBO showed an increase in the E_r value relative to the rGO membrane, indicating that due to the high concentration of the TBO molecules, the rGO-TBO layer was reinforcing the wet membrane. Additionally, the E_r values decreased for the compacted membranes in the wet state as compared to their dry counterparts at TBO loadings less than 26 wt.%. This result suggested that these compacted membranes swell when exposed to water, and the swelling decreased the transverse stiffness of the membranes. However, at 26 wt.% TBO loading, the increased H-dimer concentration hindered the swelling, since the E_r values of the compacted membranes with 26 wt.% TBO loading were statistically the same in dry and wet conditions [98].

Figure 4.5 shows the force-strain curves for non-compacted PVDF and the PVDF compacted with the hydraulic press. The PVDF support had statistically similar modulus, tensile strength and toughness values to the support which was used for the dry membrane testing. The force-strain curves of the non-compacted PVDF and the PVDF compacted with the hydraulic press do not overlap, indicating that the change in modulus of the bare support in wet state was due to both a decrease in the cross-sectional area and the effect of compaction on the material structure.

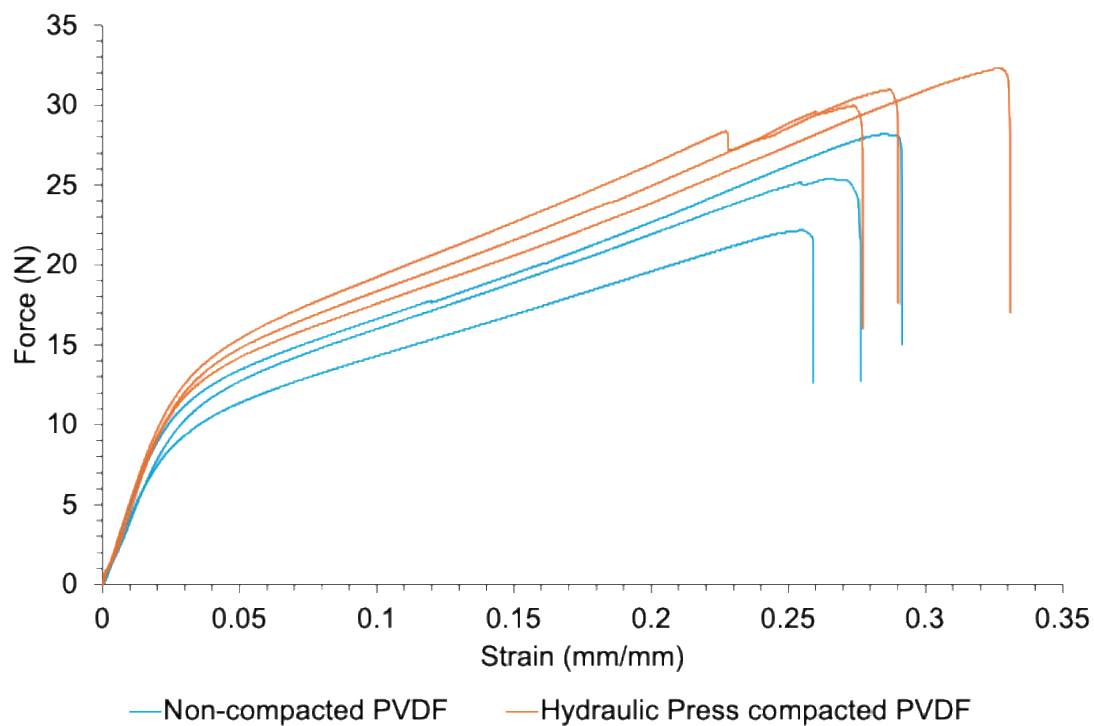


Figure 4.5: Force-strain curves of the non-compacted PVDF support and the PVDF support compacted with the hydraulic press.

The key takeaways from this chapter are:

- Compaction led to a decrease in the cross-sectional area of the membranes, thereby improving the axial mechanical properties of the PVDF supported dry membranes, in comparison to their non-compacted counterparts.
- However, the introduction of water negated the effect of compaction. The demarcation in the axial mechanical properties of the non-compacted and compacted membranes was no longer evident when the membranes were tested in the wet condition.

- For the nanoindentation measurements, the properties of the support did not dominate the E_r value results for the membranes.
- The arrangement of the TBO molecules had an impact on the E_r values of the dry non-compacted membranes, wherein the TBO molecules provided resistance to the flexure of the rGO layers at lower loadings.
- Results from nanoindentation measurements of the dry compacted membranes suggested that at 9.1 wt.% and 26 wt.% TBO loadings, the TBO molecules reach some sort of saturation, in the monomer and the dimer arrangements, respectively.
- Most of the wet compacted membranes showed a decrease in the E_r value as compared to their dry counterparts, further underscoring the effect of water on the mechanical properties of the membranes.

CHAPTER 5. COMPONENT EFFECT ON THE AXIAL AND TRANSVERSE MECHANICAL PROPERTIES OF THE DRY MEMBRANES

In this chapter, we explored how the choice of support material and its structure affected the mechanical behavior of the membrane assembly (rGO-TBO layer and support) by comparing the properties of membranes installed on PES supports to those for membranes installed on PVDF supports. To investigate the component effect further, some new intercalants besides the baseline TBO (also referred to as TZ-1) intercalant, were explored as well.

This chapter is divided into five subparts – one focusing on a new substrate, that is, testing the PES supported membranes containing only the baseline intercalant TZ-1; the other subpart focuses on the new intercalants on PES; the third part is centered around testing FS films containing different intercalants to understand the mechanical properties of the rGO/rGO-X layer independent of the polymer support; in the fourth part, micromechanical mixing models are used to estimate the composite E_r value which is then compared to the experimental values; and finally in the fifth subpart, the interfacial shear traction, which is a measure of the interfacial adhesion of the rGO/rGO-X layer on PES, is reported for a select few samples in the non-compacted state. The PES supported membranes were tested only in the dry state, since the rGO/rGO-X layer delaminated from the PES support when soaked in water. However, the adhesion of the rGO/rGO-X layer was sufficient on PES to conduct permeation measurements and serve as nanofiltration membranes.

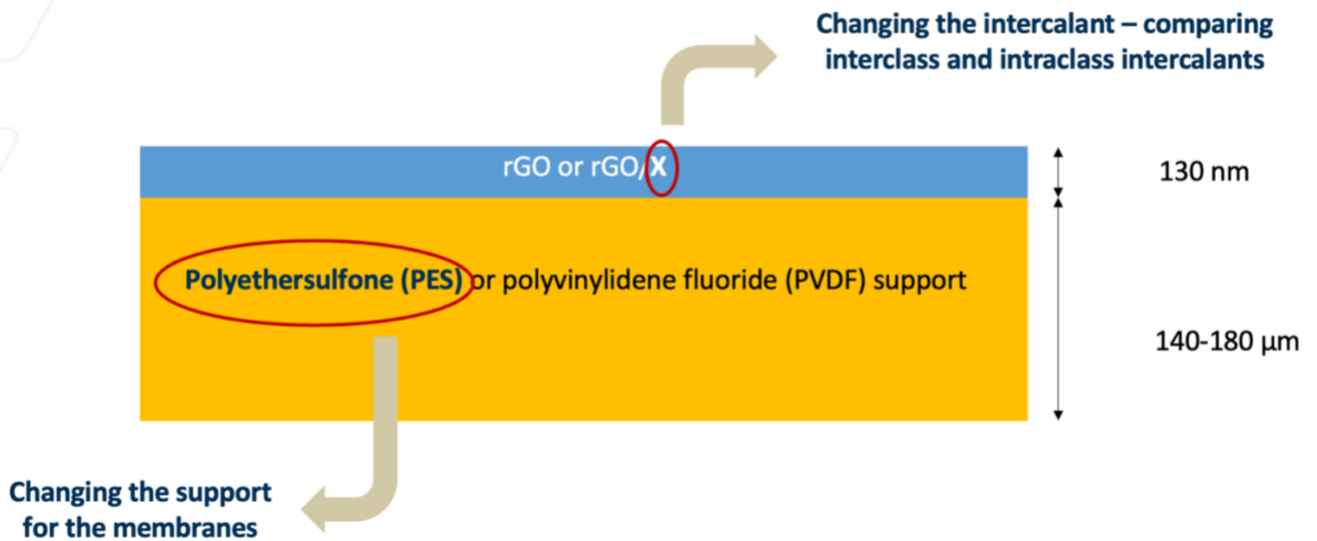


Figure 5.1: Schematic showing the components of the membranes

5.1. Effect of the substrate on the mechanical properties of the membranes. Both PES and PVDF were classified as hydrophilic materials by the supplier, and the PES support had the same nominal pore size as the PVDF support. However, the structure of the supports was different, as shown in Figure 5.2. The PVDF support had a backing material that provided additional mechanical stability, and the PES support did not. The addition of a backing material to the PVDF support meant that the PES support was more flexible at ambient conditions.

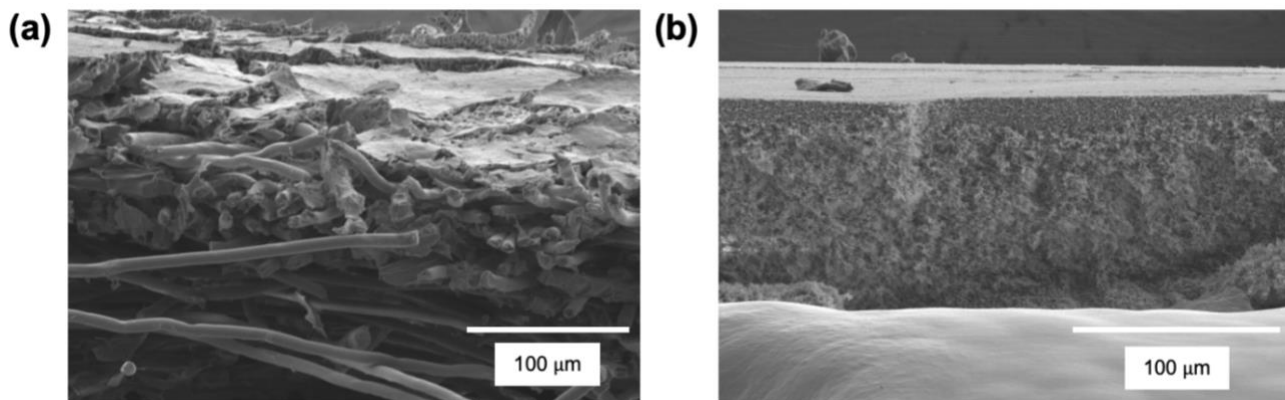


Figure 5.2: The cross-sectional SEM images of the PVDF polymer support (a), and the PES polymer support (b).

Figure 5.3 shows the modulus, tensile strength, toughness, and E_r values for the membranes on PES supports. In addition to the rGO membrane, two rGO-TBO membranes were examined containing 9.1 and 26 wt.% TBO. The PES membranes, which have a lower modulus value than the PVDF membranes, showed a similar stress-strain behavior to the latter, with the membranes elongating beyond the yield stress up to a certain tensile stress value before failing, thereby having some toughness.

For the non-compacted membranes, the modulus values were similar to the modulus values of the bare PES support, and this trend was also observed for the tensile strength and toughness values of the PES supported membranes. Compaction did not change these properties considerably. Though the modulus of the bare support material increased with compaction, the change was smaller than what was observed for the PVDF support. The differences seen between membranes on PES and PVDF supports likely correlated to differences observed in the adhesion of the rGO layer. As observed through handling the samples, the rGO and rGO-TBO layers were found to

adhere more strongly to the PVDF support, though adhesion was sufficient in both cases for use in permeation experiments. Reduced adhesion would affect the mechanical performance since load transfer between the support and rGO-based layer would be decreased, translating into no meaningful changes to the mechanical properties as measured by tensile testing. Moreover, the rGO-PES and the rGO-TBO-PES samples could not be mechanically tested in the wet condition since the rGO/rGO-TBO layer delaminated from the PES support when the wet samples were handled with tweezers. While the tensile modulus was unaffected by the addition of TBO, the E_r values, obtained from nanoindentation tests on these membranes, showed a change with TBO addition for the dry non-compacted samples. Similar to the membranes with PVDF support, the TBO molecules act as pillars, imparting stiffness to the membranes in the transverse direction and increasing the E_r values of the membranes with 9.1 wt.% and 26 wt.% TBO relative to the rGO membrane. While the transverse stiffness values of the rGO-PVDF membranes were very close in value for the non-compacted and the compacted membranes, there was a difference in the E_r values of the non-compacted and compacted rGO-PES membranes. The compacted rGO-PES membrane showed almost double the transverse stiffness as compared to its non-compacted counterpart.

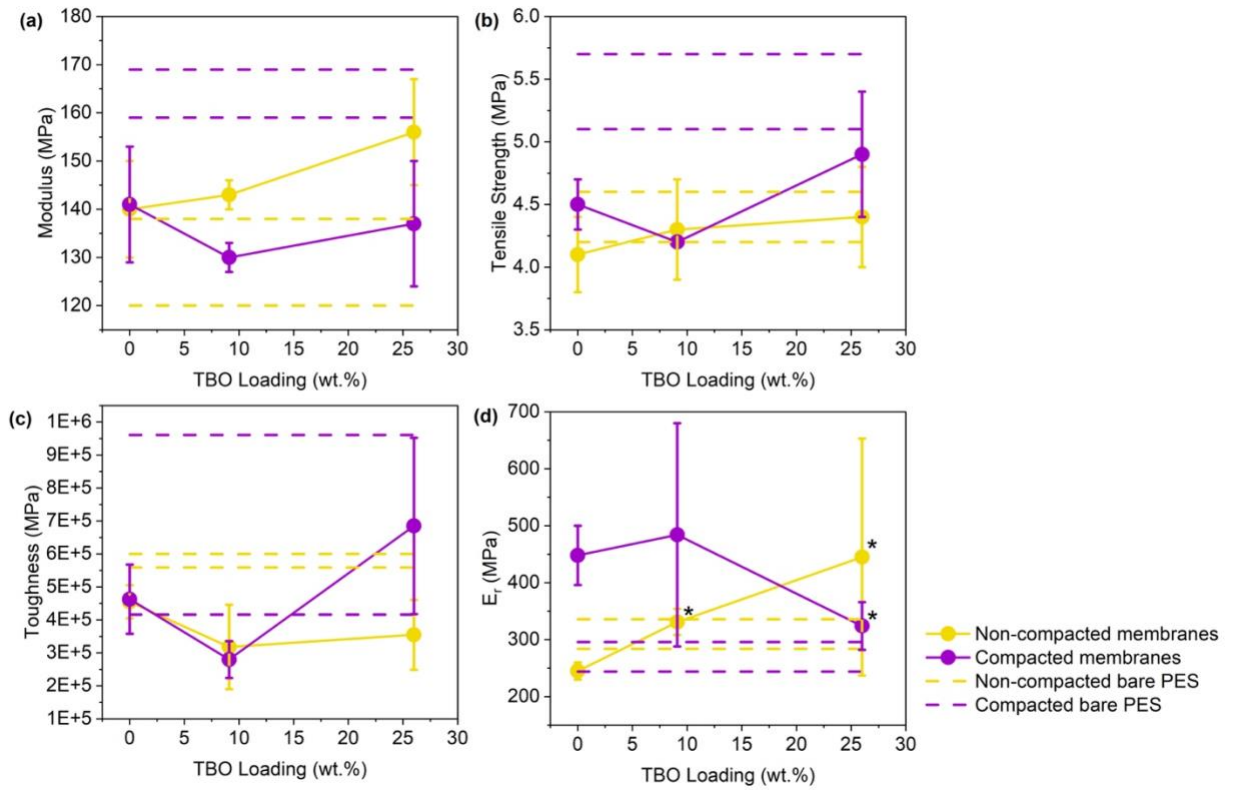


Figure 5.3: The modulus (a), tensile strength (b), toughness (c) and E_r (d) values for the dry PES supported membranes having different loadings of TBO. The asterisks (*) indicate statistically significant values when compared to the rGO-PES membranes using a t-test with a 95% confidence interval. The bare PES membrane has been shown with two dashed lines which represent the upper and lower bounds of the mechanical property obtained from the standard deviation in that property.

Figure 5.4 shows the force-strain curves of the non-compacted PES support and the PES support compacted with the hydraulic press. The force-strain curves for the non-compacted and the compacted PES overlapped indicating that the reduction in the cross-sectional area was the main

contributing factor for any changes in the modulus, tensile strength and toughness values on compaction of the PES support.

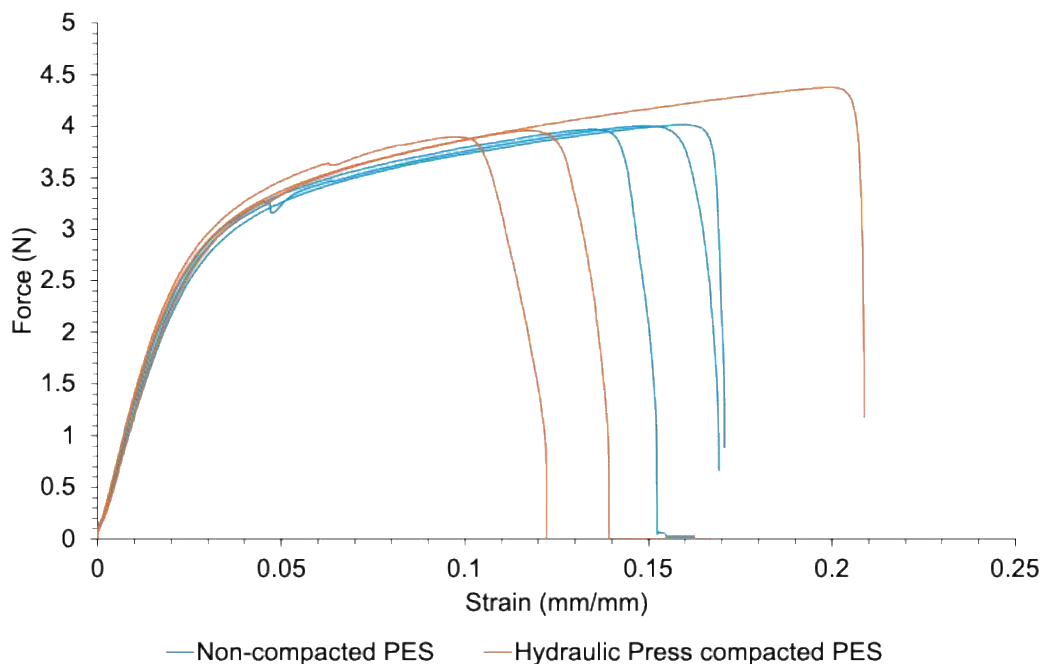
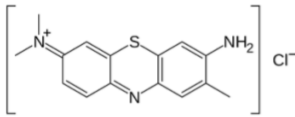
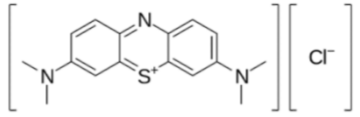
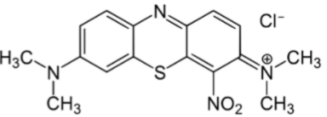
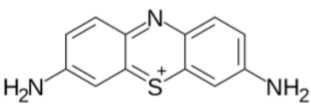
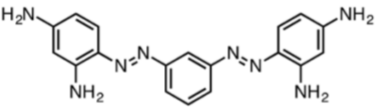
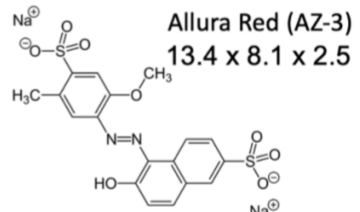
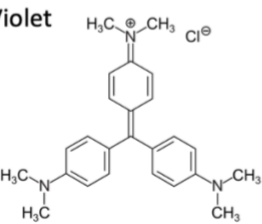
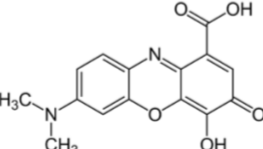
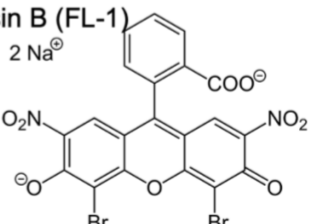


Figure 5.4: Force strain curves of the non-compacted PES support and the PES support compacted with the hydraulic press.

5.2. Effect of the intercalant on the mechanical properties of the membranes. While the substrate influenced the mechanical properties of the membranes, the intercalants were also changed to evaluate if the intercalant structure played a significant role in the mechanical behavior of the membrane. The mechanical property values for membranes containing these intercalants were measured at a loading of 9.1 wt.%. The intercalants used for this study, besides toluidine blue O (TBO or TZ-1), were methylene blue (TZ-2), methylene green (TZ-3), thionin (TZ-4), bismarck brown (AZ-1), allura red (AZ-3), crystal violet (TM-1), gallocyanin (OX-1), and eosin-B (FL-1). The ‘TZ’ intercalants had a thiazine backbone, similar to the TBO dye studied earlier. The ‘AZ’ intercalants had an azo backbone, the ‘TM’ intercalant had a triarylmethane backbone, the ‘OX’

intercalant has an oxo backbone and the 'FL' intercalant was for fluorescent red dye. The structure of these intercalants along with their dimensions are shown in Table 5.1.

Table 5.1: The different structures and dimensions of the intercalants used with the PES supported membranes. (The dye molecule dimensions were measured by Muskan Sonker in the ChBE department at Georgia Tech). The measurements are in Angstroms and were obtained using Chemdraw 3D.

<p>Toluidine Blue O (TZ-1)</p>  <p>13.1 x 6.08 x 1.8</p>	<p>Methylene Blue (TZ-2)</p>  <p>14.2 x 6.08 x 1.8</p>	<p>Methylene Green (TZ-3)</p>  <p>14.2 x 6.08 x 1.8</p>
<p>Thionin (TZ-4)</p>  <p>11.5 x 4.9 x 1.8</p>	<p>Bismarck Brown (AZ-1)</p>  <p>17.4 x 7 x 1</p>	<p>Allura Red (AZ-3)</p>  <p>13.4 x 8.1 x 2.5</p>
<p>Crystal Violet (TM-1)</p>  <p>14 x 12.2 x 1.8</p>	<p>Gallocyanin (OX-1)</p>  <p>11.5 x 6.9 x 1.8</p>	<p>Eosin B (FL-1)</p>  <p>9.8 x 11.6 x 1</p>

Different dye molecules were chosen from the same class (like TZ-1, TZ-2, TZ-3 and TZ-4 from the thiazine class, AZ-1 and AZ-3 from the azo class) so as to understand the differences in the contribution of the dyes with the same chemical backbone, to the mechanical properties of the membranes. Interclass dyes were compared as well, to understand how different chemical structures could influence the mechanical properties of the membranes. The membranes used for

this section of the study were compacted at a TMP of 50 bar. The bare PES support and the rGO-TBO on PES membrane were also compacted at a pressure of 50 bar, unlike the PES support and the rGO-TBO on PES membrane tested earlier which were compacted at 30 bar. The PES support was compacted at a pressure of 50 bar using the hydraulic press for a period of 48 hours. Tensile test results of PES-supported membranes containing these intercalants (Figure 5.5) did not show any meaningful statistical differences.

The HSN results, however, did show some differences in the E_r values of the membranes containing different intercalants. All the intercalant-containing membranes in the non-compacted state showed an increase in the E_r value relative to the rGO membrane. This increase in the transverse stiffness was a result of the pillaring effect of the intercalants, and the different levels of interactions of the intercalants with rGO. This demarcation between the non-compacted membranes with intercalants and the rGO-PES membrane was not so evident when the membranes were compacted. To study the reinforcement ‘pillaring’ effect of these intercalants better, FS films were synthesized and tested for selected intercalants.

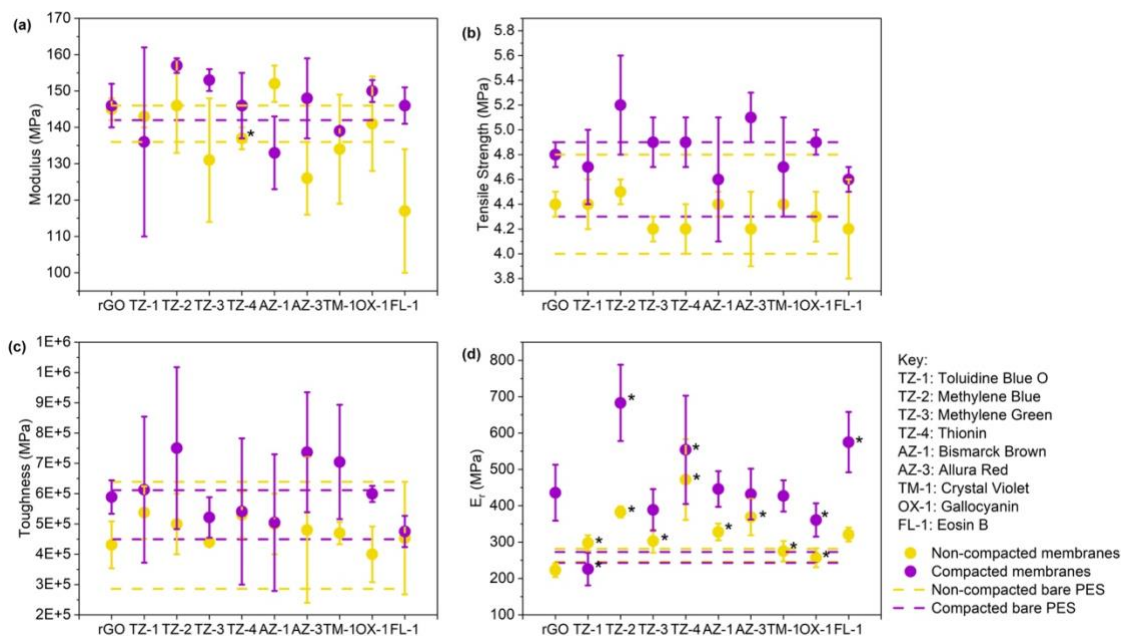


Figure 5.5: Tensile test gave the modulus values (a), tensile strength (b) and toughness (c) values, and HSN measurements gave the E_r values (d), for the PES supported membranes containing 9.1 wt.% loading of different intercalants. The asterisks (*) indicate statistically significant values when compared to the rGO-PES membranes using a t-test with a 95% confidence interval. The bare PES membrane has been shown with two dashed lines which represent the upper and lower bounds of the mechanical property obtained from the standard deviation in that property.

5.3. Free-standing (FS) rGO/rGO-X films. This section describes the results from the mechanical testing of the FS films, along with the scanning electron micrographs of these films to understand the microstructure of the rGO layers. Two loadings of rGO/rGO-X were used to make the FS films – 32 times (32FS) and 50 times (50FS) – wherein 32FS films had 32 times and 50FS films had 50 times the original amount of rGO/rGO-X used for making the membranes. Aside from the difference in the amount of rGO/rGO-X used to make the films, the 32FS and 50 FS films

were made with different vacuum pumps that applied different levels of vacuum. The 50FS films were produced using a stronger vacuum level and assembled differently as a result. The 32FS films were difficult to handle manually and could not be tested in tension. However, the 50FS films could be handled manually with tweezers, were mounted on vinyl stickers, and tested under tension. This section also shows the results from the nanoindentation testing of the 32FS and the 50 FS films, along with the tensile testing results of the 50FS films. The further analysis was done with a subset of intercalants which were TZ-1, TM-1, AZ-3 and AZ-1. Figure 5.6 shows schematically the FS film and the two types of FS films which were made with 32 times and 50 times the rGO which was used to make the membranes.

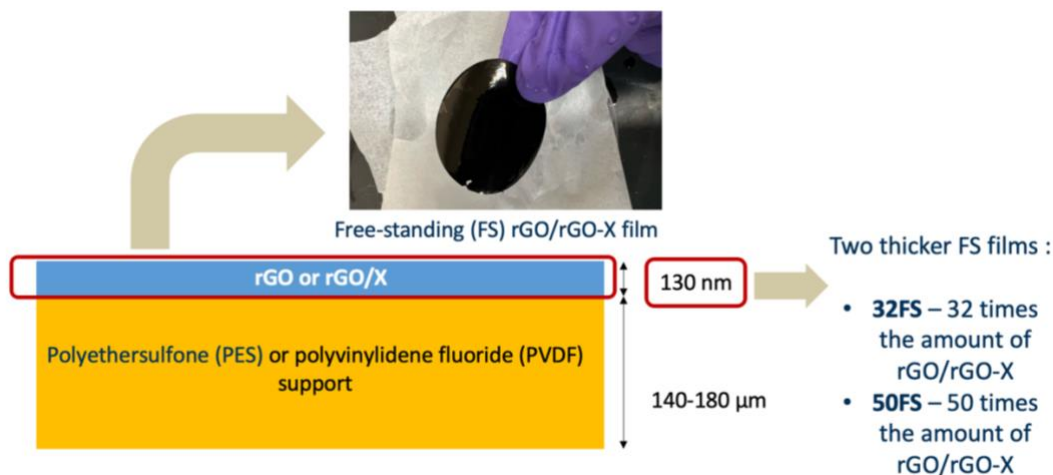


Figure 5.6: Schematic showing the FS rGO/rGO-X film

5.3.1. Scanning electron micrographs of the FS films

First, to understand the stacking behavior of rGO, SEM images of the FS films were taken as per the description provided in the Methods chapter. The stacking behavior of the rGO layers changed as the vacuum filtration process progressed (Figure 5.6). This stacking nature of rGO could be

seen in the cross-sectional SEM images of the 32FS rGO film. Initially, the layers of rGO were stacked closely together, and as the vacuum filtration progressed, the layers were more loosely packed. The stacking behavior of the 32FS film would be expected to influence the transverse mechanical properties of the 32FS films.

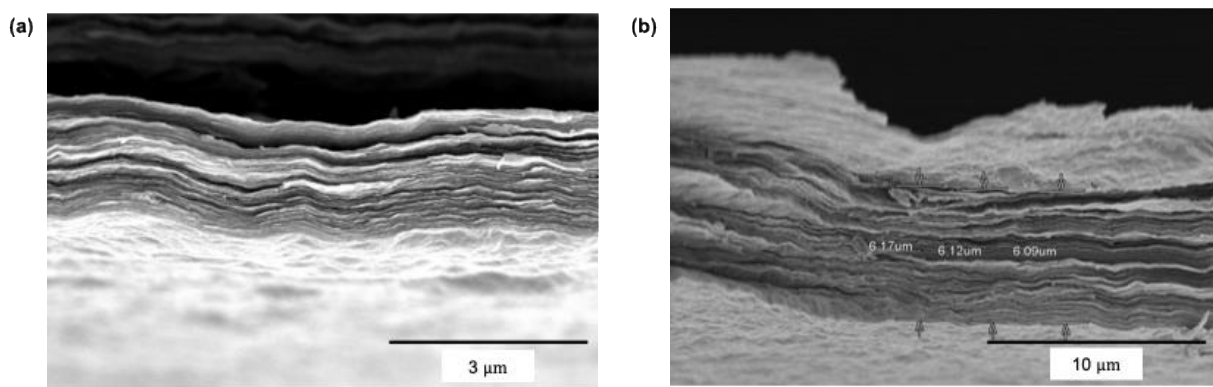


Figure 5.7: The cross-sectional SEM images (a) and (b) of the 32FS rGO film.

The rGO layers are closely packed together initially, and as the vacuum filtration process progresses, the spacing between the rGO layers increases. Figure 5.8 shows the scanning electron micrographs of the 50FS films. The FS films, being brittle in nature, were easily prepared for SEM imaging.

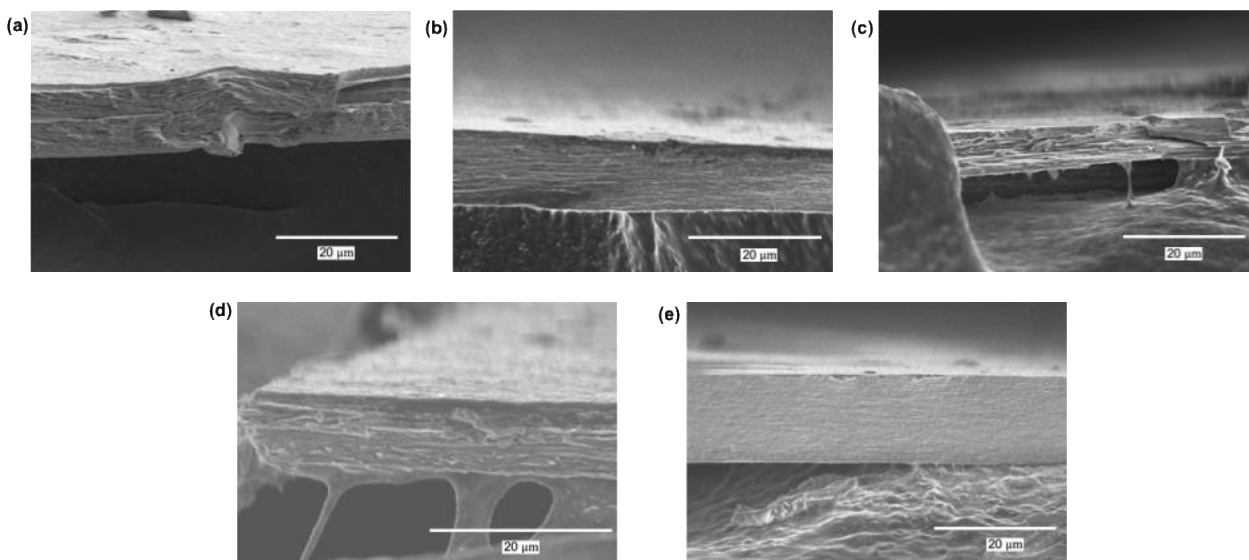


Figure 5.8: The cross-sectional SEM images of the 50FS rGO (a), rGO-Z-1 (b), rGO-TM-1 (c), rGO-AZ-3 (d), and rGO-AZ-1 (e) films.

Table 5.2 shows the thickness values of the 50FS films, calculated as an average of at least 10 different thickness values obtained by cross-sectional SEM. Considering these thickness values, the rGO film had a thickness value similar to the film containing the TM-1 intercalant. The other films, containing TZ-1, AZ-1 and AZ-3 intercalants, were thicker in comparison to the FS rGO film. These changes in film thickness did not correspond to the expected thickness dimensions of the intercalants (Table 5.2), suggesting these changes were related to different levels of interactions between rGO and the intercalants or different types of stacking of the intercalants. Per chemical models, the thickness of the intercalants was related in the following order: $AZ-1 < TM-1 = TZ-1 < AZ-3$. The thickness values could imply that the films containing the TZ-1, AZ-3 and AZ-1 intercalants were not packing as tightly as the FS rGO or the FS rGO-TM-1 films.

Table 5.2: Thickness values of the 50FS films obtained by cross-sectional SEM.

Sample	Thickness (h) (μm)
FS rGO	8.4 ± 0.7
FS rGO-TM-1	6.6 ± 0.7
FS rGO-TZ-1	11.0 ± 0.8
FS rGO-AZ-3	14.5 ± 0.8
FS rGO-AZ-1	15.1 ± 0.5

5.3.2. Small-scale tensile testing of the FS films

The 50FS films, easy to handle manually with tweezers, were tested in tension using a small-scale tensile testing load frame as described in the Methods chapter. This set-up used a 1N load cell and the sample mounting is shown in Figure 5.9.

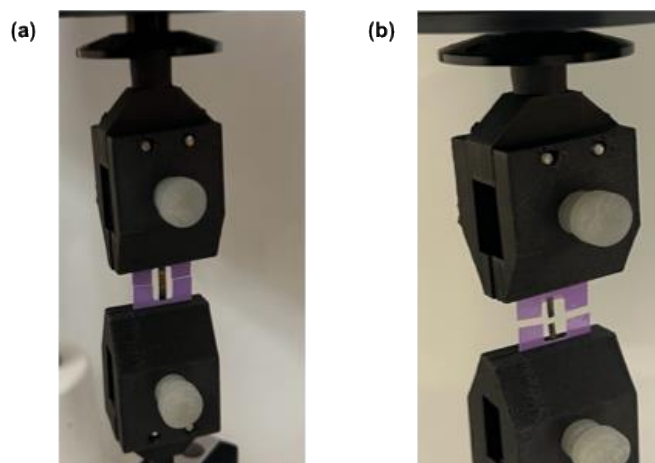


Figure 5.9: Experimental set-up to test FS films under tension before testing (a), and after fracture (b). The clamps holding the film were specifically fabricated to be compatible with a 1N load frame. The FS films were mounted using vinyl stickers (purple).

The fracture stress values obtained from the tensile testing are given in Table 5.3. Comparing the fracture stress of the intercalant containing films, as the thickness increased from TM-1 to AZ-1, the fracture stress decreased, further implying that the films containing the TZ-1, AZ-3 and AZ-1 intercalants were not packing as tightly as the FS rGO or the FS rGO-TM-1 films. This fracture stress value is used in the next part of this chapter to find the interfacial shear traction of the rGO/rGO-X layer on the PES support. The 50FS rGO film showed the highest modulus value. Among the 50FS films containing intercalants, the film with TZ-1 was the stiffest, followed by the film containing TM-1. The AZ intercalants which behaved similarly having close modulus values. The films containing the AZ intercalants were less stiff and could withstand a lower stress value before fracture, as compared to the films containing TZ-1 and TM-1.

Table 5.3: The fracture stress and modulus values of the 50FS rGO/rGO-X films when tested in tension. The fracture stress values are reported as an average of at least 2 values.

Sample	Fracture stress (σ_{frac}) (MPa)	Modulus (MPa)
FS rGO	29 ± 13	1500 ± 707
FS rGO-TZ-1	52 ± 19	1333 ± 577
FS rGO-TM-1	97 ± 33	1000 ± 0
FS rGO-AZ-3	20 ± 6	567 ± 115
FS rGO-AZ-1	19 ± 9	633 ± 58

Figure 5.10 shows the representative stress-strain curves for the 50FS films tested in tension. The shape of these curves is different as compared to those of the supported membranes. The stress-strain curves show a steep rise as the FS film is stretched under tension, followed by a

drop in stress at the end of elastic deformation. The film continued to undergo some amount of stretching before it failed or broke completely in two parts.

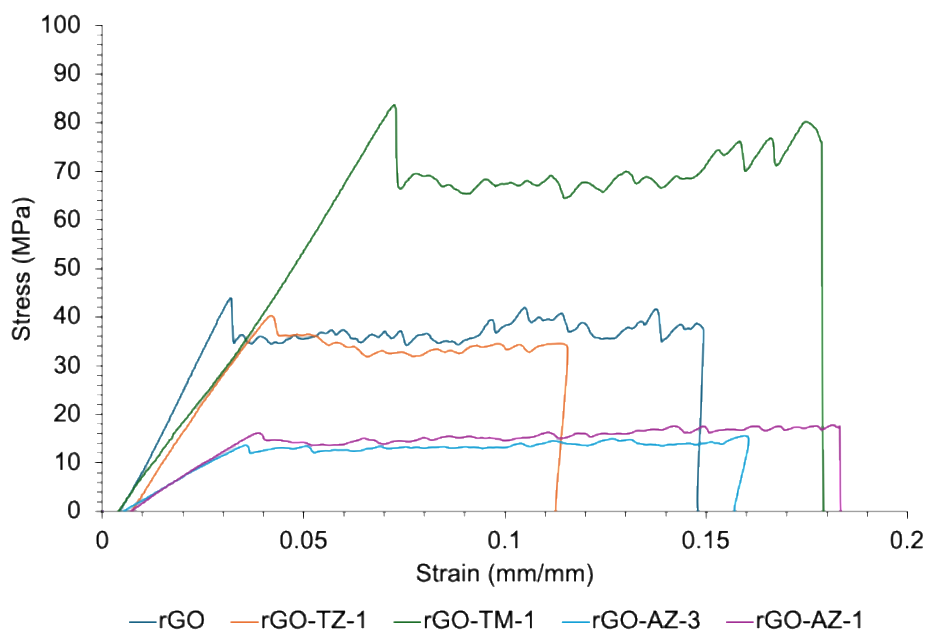


Figure 5.10: Representative stress-strain curves for the 50FS films tested in tension.

5.3.3. Nanoindentation of the FS films

Table 5.4 shows the reduced modulus (E_r) values obtained via nanoindentation performed on the two sides of the 32FS and 50FS films, wherein one side (the lower side) was in contact with the MCE membrane filter during vacuum filtration. The value of E_r represents the average value obtained from 10 indents. Two locations on the films were examined on each side.

For the other intercalant containing 50FS films, the average E_r values obtained from both locations of nanoindentation were statistically similar as seen from the E_r values reported here. However, for the FS rGO and the FS rGO-TZ-1 films, the E_r values obtained from both locations of

nanoindentation were statistically different, suggesting greater spatial variability in properties of these films.

Table 5.4: E_r values obtained by nanoindentation of the upper and lower sides of the 50FS films and the 32FS films.

Sample	Lower side E_r of 50FS films	Lower side E_r of 32FS films	Upper side E_r of 50FS films	Upper side E_r of 32FS films
FS rGO (location 1)	1.4 ± 0.1	1.3 ± 0.1	1.7 ± 0.2	0.5 ± 0.1
location 2	1.2 ± 0.1	1.3 ± 0.2	1.6 ± 0.1	0.4 ± 0.0
FS rGO-TZ-1 (location 1)	1.3 ± 0.1	1.2 ± 0.2	2.0 ± 0.1	1.7 ± 0.1
location 2	1.5 ± 0.1	1.3 ± 0.2	1.6 ± 0.1	1.4 ± 0.1
FS rGO-TM-1 (location 1)	2.6 ± 0.2	1.5 ± 0.1	2.5 ± 0.2	1.7 ± 0.2
location 2	2.6 ± 0.1	1.3 ± 0.1	2.4 ± 0.2	1.0 ± 0.2
FS rGO-AZ-3 (location 1)	2.7 ± 0.3	1.9 ± 0.1	2.7 ± 0.3	2.2 ± 0.2
location 2	2.5 ± 0.2	1.9 ± 0.2	2.5 ± 0.2	2.2 ± 0.1

The E_r values for both locations of nanoindentation of the 32FS films were not statistically similar for all samples. Additionally, the E_r values obtained from nanoindentation of the 32FS rGO film were larger for the lower side of the film in comparison to the upper side. This difference in E_r values was likely related to the arrangement of the rGO flakes as they are deposited on the MCE membrane filter. Initially as shown in Figure 5.5, the rGO was organized in a more compact

fashion and formed stacked layers, but as the vacuum filtration progressed, the arrangement may have been less ordered as the MCE filter was already covered by a continuous layer of rGO. This difference in deposition would result in the lower side being stiffer than the upper side of FS rGO film.

However, this demarcation in E_r values between the upper and the lower sides of the FS rGO film was reduced for the 50FS rGO film, with the E_r values for the two sides being closer in value. As stated previously, the vacuum pumps used to fabricate the 32FS films and the 50FS films were different, with the pump used to make the 50FS films pulling a higher vacuum than the one used to make the 32FS films. This difference in the vacuum being pulled would cause a difference in the observed E_r values. Another key takeaway from Table 5.4 was that the TM-1 and AZ-3 intercalant containing 50FS films, all had a higher E_r value in comparison to that of the 50FS rGO film. This result indicated that the intercalants, TM-1, and AZ-3 acted as pillars, reinforcing the FS films in the transverse direction. Also, the 50FS films containing intercalants showed a greater E_r value than their corresponding 32FS films, which could be attributed to the difference in the vacuum pump being used, with a stronger vacuum ensuring more packing and hence a greater transverse stiffness for the 50FS films. The 50FS films were made using the same vacuum conditions as the supported membranes and these films provide a reasonable estimation of the microstructural effect of the intercalants on the mechanical properties of the membranes.

5.4 Modeling. In addition to experimental work, modeling approaches were pursued to understand the component interactions and mechanical behavior better. We fitted the inverse rule of mixtures to the nanoindentation data for the polyether sulfone (PES) supported samples. A modification of the inverse rule of mixtures, called the Bull model, which took into consideration the indentation

test parameters, was fitted to the data as well. The values obtained from modeling, and how these compare to the experimental values, are shown in Figure 5.11.

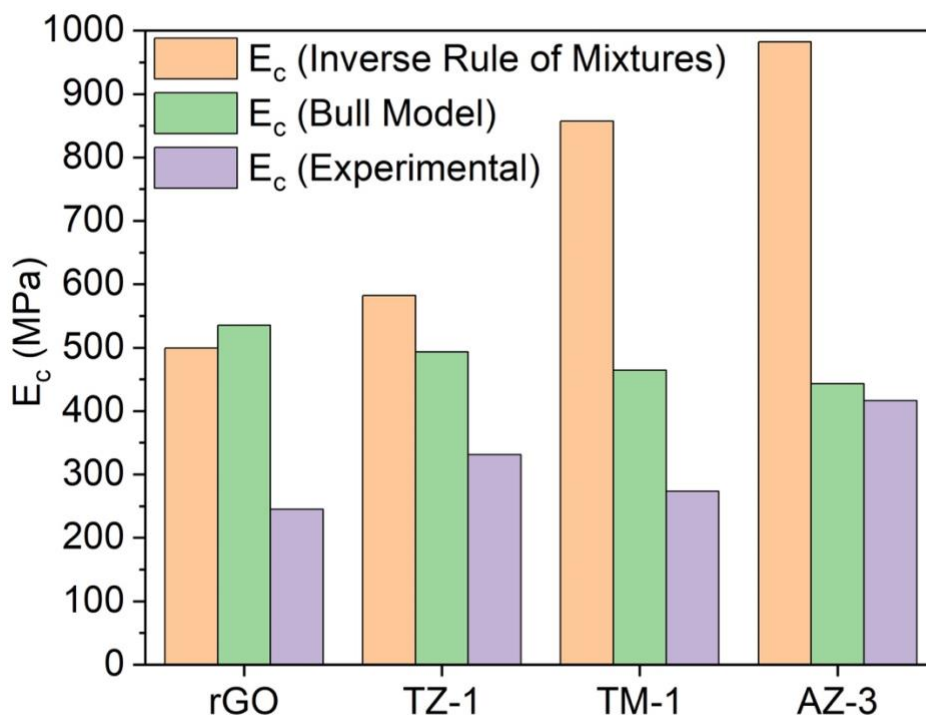


Figure 5.11: The experimental values of E_c and how these values compare to the E_c values obtained by fitting the different models.

The Bull model predicted values close to the experimental values for all the intercalant-containing samples, with the Bull model prediction being very close to the experimental value for the AZ-3 containing membrane. There are some discrepancies since the trends of the experimental data do not match the trends predicted by the models. Analyzing the results in detail, the values obtained via the inverse rule of mixtures depended heavily on the volume fractions of rGO/rGO-X and PES,

with the rGO and the TZ-1 containing membranes having similar volume fractions of the rGO/rGO-X layer. However, the volume fraction of the rGO-X layer increased significantly for the TM-1 and the AZ-3 containing membranes, thereby predicting lower composite transverse modulus values. The values predicted by the Bull model on the other hand, depend inversely on the 't_g' value, that is, the thickness of the rGO/rGO-X layer. The t_g values are higher for the TM-1 and the AZ-3 containing samples as compared to the rGO and the TZ-1 samples, thereby predicting a lower transverse stiffness value for the former samples as compared to those of the latter. The trend of values predicted by the two models are opposite, with the inverse model giving a predicting values as : AZ-3>TM-1>TZ-1>rGO, and the Bull rule predicting values as: rGO>TZ>1>TM-1>AZ-3. Since the predictions from these models were still higher than the experimentally measured values, the modeling results suggested that the load transfer between the rGO or rGO-X layer and the support as well as load transfer between rGO flakes may not be optimum. The discrepancy between the Bull model results and the experimental results decreased for the intercalant containing membranes in comparison to the rGO membrane, which could indicate better interfacial adhesion/interactions brought about by the intercalants.

While the models assumed a perfect interface between the rGO/rGO-X layer and the polymer support, the two models did not predict similar values for the intercalant containing membranes. The models do not elucidate the contribution of the polymer support. The E_g and the E_p values were found experimentally by performing nanoindentation on the FS film and the polymer support respectively. The inverse rule of mixtures calculated the volume fractions of the rGO layer and the support from the thickness measurements of the two components. The Bull model used the nanoindentation geometry parameters to predict the composite transverse modulus. However, only the indented volume was considered and not the entire membrane volume. One possible way to

optimize these model predictions would be to find an accurate way to calculate the volume fractions of the rGO layer and the polymer support.

5.5 Interfacial shear traction of the rGO/rGO-X layer on PES support. The fragmentation test was used to quantify the shear traction between the rGO/rGO-X layer and the polymer (PES) support, wherein a higher value of the shear traction translates into greater interfacial adhesion between the rGO/rGO-X layer and the polymer support, as per equation 7 ($\tau_{\max} = \frac{3}{4} \pi \frac{h}{\lambda} \sigma_{\text{frac}}$). The value of the thickness of the rGO/rGO-X layer (h) was found by measuring the thickness of the 50FS films and the fracture stress value (σ_{frac}) was found by fracturing the 50FS films under tension. To obtain the mean spacing between cracks, λ , a line was drawn on the images perpendicular to the fragmentation cracks, and the number of cracks that crossed this line were counted. This value was used to calculate λ . This procedure of calculating the shear traction has been described in the Methods chapter. Figure 5.12 schematically elucidates the interface between the rGO/rGO-X layer and the PES support.

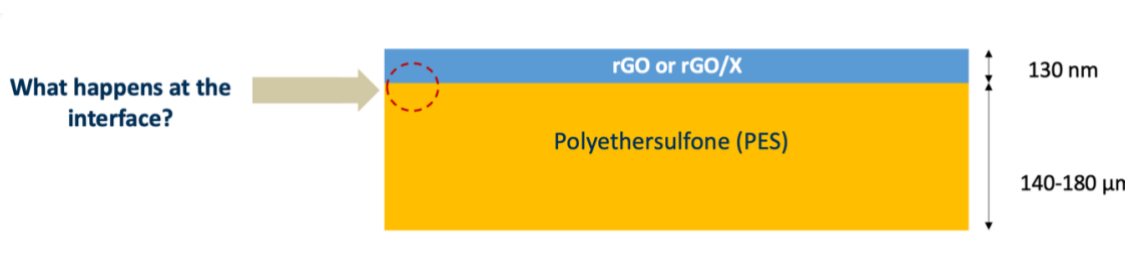


Figure 5.12: Schematic to show the interface between the rGO/rGO-X layer and the PES support.

Using the data shown in Table 5.3, the fragmentation testing dataset was completed for the edge location of the fragmented samples. The results of the interfacial shear traction for the samples are shown in Figure 5.13. The values of the interfacial shear traction, which are indicative of the

adhesive strength of the rGO/rGO-X layer on the polymer support, are reported in kPa. Figure 5.10 shows the values of the interfacial shear traction for the non-compacted samples since the FS films were tested in the non-compacted state.

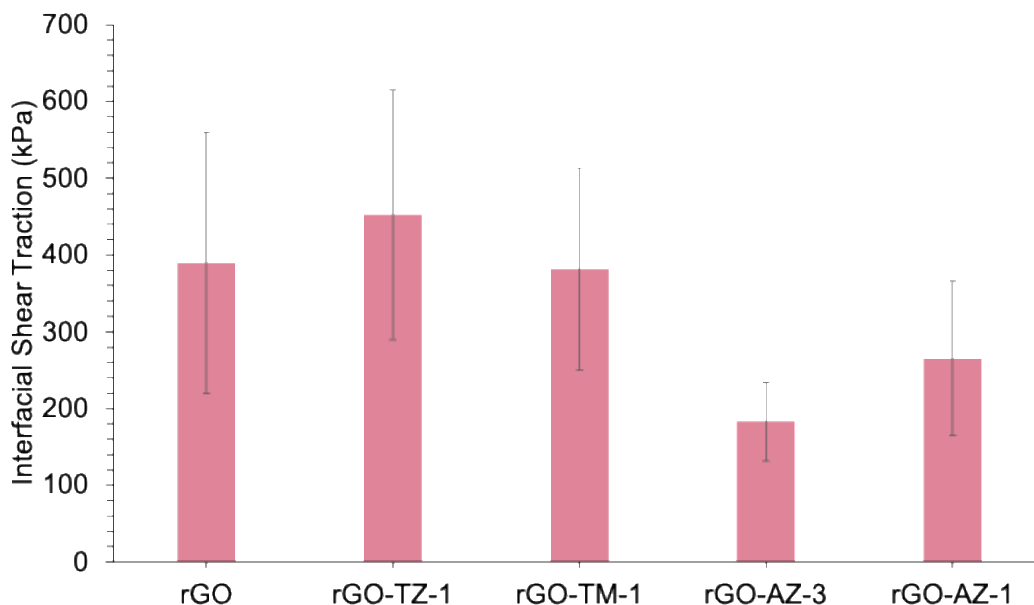


Figure 5.13: The interfacial shear traction versus the non-compacted fragmented sample.

Observing Figure 5.11, the rGO, rGO-TM-1, and rGO-TZ-1 membranes had similar values of interfacial shear traction, with the TZ-1 containing membrane showing a slightly greater adhesion value than the other two membranes. The AZ intercalants behaved similarly to each other, with AZ-1 and AZ-3 containing membranes having lower adhesion as compared to the other membranes. The overall trends in interfacial shear traction for non-compacted membranes did not correlate definitively with the compacted membrane performance trends. The behavior of the AZ intercalants was similar for the fracture stress and the modulus values, and the same trend was observed for the interfacial shear traction values as well. Extrapolating the trends in the shear

traction values to the compacted membranes could suggest that the TZ-1 and TM-1 intercalants are more robust in operation as compared to the AZ intercalants.

Key takeaways from this chapter:

- The PVDF support used in this work had a fibrous microstructure, rendering the PVDF supported membranes stiffer than the PES supported membranes.
- The rGO/rGO-TBO layer adhered more strongly to the PVDF support than the PES support. This means that the load transfer between the rGO/rGO-TBO layer and PES was decreased, leading to no meaningful changes in the axial mechanical properties of the PES-supported membranes.
- The difference in the mechanical behavior of the different intercalants was not clear from the tensile tests or from the HSN measurements. To understand the behavior of some of the intercalants of particular interest, the free-standing (FS) films of these intercalants were fabricated and tested.
- Measuring the thickness of the 50FS films helped to bring out the difference in the stacking behavior of the different intercalants. The 50FS film containing TM-1 was the thinnest and was thinner than rGO. The 50FS films containing the TZ-1, AZ-3 and AZ-1 were thicker, implying that these films were not as tightly packed as the rGO and the rGO-TM-1 films. This difference in thickness did not correlate with the thickness of the intercalants obtained by chemical modeling, indicating that the intercalants could be arranged differently in the rGO galleries.
- The results of nanoindentation of supported membranes showed that the intercalant containing films had a higher transverse stiffness (E_r value) as compared to the rGO

membrane. The nanoindentation test results of the 50FS films aligned with this observation, wherein the TM-1 and AZ-3 intercalant containing films had higher E_r values than the rGO film. This behavior indicated that the intercalants acted as pillars, reinforcing the supported membranes and the FS films, and the differences in stacking or the interactions with rGO were discernable for this measurement.

- The results of tensile tests of supported membranes did not show substantial differences in the axial mechanical properties. However, 50FS films did show differences in fracture stress. The tensile tests of the supported membranes gave mechanical property values that were influenced by the PES support, whereas the 50FS films provided different information regarding the rGO/rGO-X layer independent of the support. Among the intercalants explored in the FS films, TM-1 had the highest fracture stress followed by TZ-1, AZ-3 and AZ-1, with the AZ intercalants behaving similarly. Since the fracture stress would be related to interactions between the intercalants and the rGO, this trend showed that the different classes of intercalants interacted with rGO differently. Following this logic, the TM-1 intercalant showed the strongest interaction with rGO.
- The TZ-1 containing membrane showed the highest adhesion strength, with the TM-1 and the rGO membranes close in value. The AZ intercalants behaved similar to each other, showing substantially lower adhesion strength as compared to TZ-1 and TM-1.
- The chemical structure or the level of interaction of the intercalant with rGO could have played a role in determining the adhesion strength for these non-compacted membranes. Extrapolating to the compacted membranes, these results could suggest that the TZ-1 and the TM-1 membranes are more robust in operation.

CHAPTER 6. CONCLUSION AND FUTURE WORK

6.1. Conclusion

This project set out to understand the mechanical properties of PVDF and PES supported rGO membranes and was successful in quantifying the key mechanical properties – modulus, tensile strength, toughness, transverse modulus and the interfacial adhesion. Compacted PVDF supported membranes were stiffer as compared to their non-compacted counterparts due to a reduction in the cross-sectional area, and this effect of compaction was negated by the introduction of water in the membrane structure. TBO, arranged in different stacked forms, primarily monomers and dimers, had an influence on the membrane mechanics. Nevertheless, the TBO molecules acted as pillars, reinforcing the membrane in the transverse direction, as observed from the nanoindentation experiments.

While the mechanical properties of the PVDF supported membranes were understood extensively, another focus of this research was exploring the component effect. The polymer support was changed from PVDF to PES, and a new set of intercalants were used along with TBO. PES supported membranes were less stiff than their PVDF counterparts, due to the difference in the microstructures of the two polymers. Moreover, the rGO/rGO-X layer did not adhere as strongly to PES as it did to PVDF. This decrease in adhesion strength meant that no statistically significant changes were observed in the mechanical properties of the dry PES membranes as the loading of TBO was increased.

The results of tensile tests of supported membranes did not show substantial differences in the axial mechanical properties. However, 50FS films did show differences in fracture stress. The tensile tests of the supported membranes gave mechanical property values that were influenced by the PES support, whereas the 50FS films provided different information regarding the rGO/rGO-X layer independent of the support. Among the intercalants explored in the FS films, TM-1 had the highest fracture stress followed by TZ-1, AZ-3 and AZ-1, with the AZ intercalants behaving similarly. Since the fracture stress would be related to interactions between the intercalants and the rGO, this trend showed that the different classes of intercalants interacted with rGO differently. Following this logic, the TM-1 intercalant showed the strongest interaction with rGO.

The rGO/rGO-X layer showed a stacked structure when viewed under SEM. The changes in this stacked structure due to intercalants from the supported membranes were difficult to isolate. However, measuring the thickness of the 50FS films helped to bring out the difference in stacking with different intercalants. The 50FS film containing TM-1 was the thinnest and was thinner than rGO. The 50FS films containing the TZ-1, AZ-3 and AZ-1 were thicker, implying that these films were not as tightly packed as the rGO and the rGO-TM-1 films. This difference in thickness did not correlate with the thickness of the intercalants obtained by chemical modeling, indicating that the intercalants could be arranged differently in the rGO galleries.

While TBO (TZ-1) served as the baseline intercalant, the new intercalant chemistries and their interactions with rGO governed the mechanical behavior of these FS films. The 50FS films containing TM-1 and AZ-3 intercalants showed a higher transverse stiffness value as compared to the TZ-1 containing FS film and the rGO film, since the TM-1 and the AZ-3 intercalants acted as pillars, resisting the flexure of the rGO layers.

Fragmentation test results shed light on the adhesion strength of the rGO/rGO-X layer on PES, with TM-1 and TZ-1 intercalants displaying the highest adhesion strength, suggesting that these could be more robust in operation. The AZ-1 and AZ-3 intercalants behaved similarly and showed a significantly less adhesion strength value in comparison to the TM-1 and TZ-1 intercalants. While the inverse rule of mixtures overpredicted the composite transverse modulus values, the Bull model was successful in predicting values closer to the experimental values, especially for the TM-1 and AZ-3 intercalant containing membranes.

6.2. Future Work

The next steps of this research project involve a deeper understanding of the rGO/rGO-X layer and the polymer interface, for which some preliminary nanoscratch experiments were performed. Nanoscratch technique was introduced in the year 1950 and since then it has transformed from a qualitative test to a quantitative test to find the adhesive strength of coatings on substrates. In the nanoscratch test, an indenter scratches the dry membranes at a fixed speed and with a critical load, generating the value of the coefficient of friction. The equation shown below, known as the Laugier formula, is used to calculate the adhesive strength of the coating/top layer on the substrate:

$$\text{Adhesive Strength } (\sigma_a) = \frac{2P_c}{\pi d_c^2} \left[(4 + \nu_s) \frac{3\pi\mu}{8} - (1 - 2\nu_s) \right]$$

where, σ_a is the adhesive strength, P_c is the critical contact load, d_c is the residual scratch width, ν_s is Poisson's ratio of the substrate, and μ is coefficient of friction (obtained from the software during testing).

After performing the scratch, the software provided multiple curves, out of which two were of particular interest to us. The normal force versus time plot indicates the maximum load used to perform the scratch. The normal displacement versus time plot indicates the maximum depth up to which the indenter penetrates the sample while performing the scratch. The other parameters of the Laugier expression include the Poisson's ratio of the polymer substrate and the residual scratch width. After finding the parameters of the Laugier formula, it can be applied to find the adhesive strength between the rGO layer and the polymer support [110-116].

Another area of interest could be developing FS films of different thicknesses and with different loadings of intercalants, to gain a deeper understanding of the FS mechanics. The 32FS and the 50FS films showed different mechanical performance, and fabricating films of different thickness could help gain insight into how the loading of rGO/rGO-X can influence the mechanical properties of these FS films. Finally, a better fitting inverse model, which can predict the values closer to the experimental values for all the intercalant containing films, needs to be identified or developed. Building such a model can help predict how including different intercalants could affect the mechanical properties of the polymer supported rGO membranes.

REFERENCES

1. Bai, Z.S., Wang, H.L., *Crude oil desalting using hydrocyclones*. Chemical Engineering Research and Design, 2008. **85**(12): p. 1586-1590.
2. Pereira, J., Velasquez, I., Blanco, R., Sanchez, M., Pernalete, C. and Canelón, C. *Crude oil desalting process*. 2015. 1-11.
3. Riazi, M., Eser, S., Agrawal, S.S. and Díez, J.P., *Crude oil refining processes*, in *Petroleum Refining and Natural Gas Processes*, S.E. M R Riazi, J L Peña, Editor. 2013, ASTM eBooks. p. 103-104.
4. Sun, P., Elgowainy, A., Wang, M., Han, J. and Henderson, R.J., *Estimation of U.S. refinery water consumption and allocation to refinery T products*. Fuel, 2018. **221**: p. 542-557.
5. Strathmann, H., *Introduction to membrane science and technology*. John Wiley & Sons, 2011: p. 1-87.
6. Strathmann, H., *Membrane separation processes: current relevance and future opportunities*. AIChE journal, 2001. **47**(5): p. 1077-1087.
7. Valero, F., Barceló, A. and Arbós, R., *Electrodialysis technology: theory and applications*. Desalination, Trends and Technologies, 2011. **28**: p. 3-20.
8. Strathmann, H., *Electrodialysis and related processes*. In *Membrane science and technology* Elsevier, 1995. **2**: p. 213-281.
9. Bowry, S.K., *Dialysis membranes today*. The International Journal of Artificial Organs, 2002. **25**(5): p. 447-460.
10. Stichlmair, J.G., Klein, H. and Rehfeldt, S., *Distillation: principles and practice*. 2021: John Wiley & Sons. 1-75.

11. Mallakpour, S., Azadi, E., *Nanofiltration membranes for food and pharmaceutical industries*. Emergent Materials, 2022. **5**(5): p. 1329-1343.
12. Matsuura, T., *Progress in membrane science and technology for seawater desalination—a review*. Desalination, 2001. **134**(1-3): p. 47-54.
13. Zhao, F.Y., An, Q.F., Ji, Y.L. and Gao, C.J, *A novel type of polyelectrolyte complex/MWCNT hybrid nanofiltration membranes for water softening*. Journal of Membrane Science, 2015. **492**: p. 412-421.
14. Khan, F.S.A., Ahmed, S., Karri, R.R., Mubarak, N.M., Jatoi, A.S., Khalid, M., Tan, Y.H., Khan, N.A. and Koduru, J.R., *Nanofiltration membranes for wastewater treatment and biotechnological applications*. In Hybrid Nanomaterials for Sustainable Applications Elsevier, 2023: p. 321-337.
15. Lau, W.J., Ismail, A.F., *Polymeric nanofiltration membranes for textile dye wastewater treatment: preparation, performance evaluation, transport modelling, and fouling control—a review*. Desalination, 2009. **245**(1-3): p. 321-348.
16. Lee, A., Elam, J.W. and Darling, S.B., *Membrane materials for water purification: design, development, and application*. Environmental Science: Water Research & Technology, 2016. **2**(1): p. 17-42.
17. Pera-Titus, M., *Porous inorganic membranes for CO₂ capture: present and prospects*. Chemical Reviews, 2013. **114**(2): p. 1413-1492.
18. Tul Muntha, S., Kausar, A. and Siddiq, M., *Advances in polymeric nanofiltration membrane: A review*. Polymer-Plastics Technology and Engineering, 2017. **56**(8): p. 841-856.
19. Yang, Z., Zhou, Y., Feng, Z., Rui, X., Zhang, T. and Zhang, Z., *A review on reverse osmosis and nanofiltration membranes for water purification*. Polymers, 2019. **11**(8): p. 1252.

20. Wang, Z., Luo, X., Zhang, J., Zhang, F., Fang, W. and Jin, J., *Polymer membranes for organic solvent nanofiltration: Recent progress, challenges and perspectives*. *Advanced Membranes*, 2023. **3**: p. 100063.
21. Lau, W.J., Ismail, A.F., Goh, P.S., Hilal, N. and Ooi, B.S., *Characterization methods of thin film composite nanofiltration membranes*. *Separation & Purification Reviews*, 2015. **44**(2): p. 135-156.
22. Ismail, A.F., Padaki, M., Hilal, N., Matsuura, T. and Lau, W.J., *Thin film composite membrane—Recent development and future potential*. *Desalination*, 2015. **356**: p. 140-148.
23. Seah, M.Q., Lau, W.J., Goh, P.S., Tseng, H.H., Wahab, R.A. and Ismail, A.F., *Progress of interfacial polymerization techniques for polyamide thin film (nano) composite membrane fabrication: a comprehensive review*. *Polymers*, 2020. **12**(12).
24. Zare, S., Kargari, A., *Membrane properties in membrane desalination*, in *Emerging Technologies for Sustainable Desalination Handbook*, . 2018, Elsevier.
25. Zinadini, S., Zinatizadeh, A.A., Rahimi, M., Vatanpour, V. and Zangeneh, H., *Preparation of a novel antifouling mixed matrix PES membrane by embedding graphene oxide nanoplates*. *Journal of Membrane Science*, 2014. **453**: p. 292-301.
26. Mohammad, A.W., Teow, Y.H., Chong, W.C. and Ho, K.C., *Hybrid Processes: Membrane Bioreactor*. In *Membrane Separation Principles and Applications*, 2019: p. 401-470.
27. Dallaev, R., Pisarenko, T., Sobola, D., Orudzhev, F., Ramazanov, S. and Trčka, T., *Brief review of PVDF properties and applications potential*. *Polymers*, 2022. **14**(22): p. 4793.
28. Vance, J., Shaw, A. and Delzeit, L., *Engineering Polymers as Structural Materials in Spacecraft Water Systems*, in *51st International Conference on Environmental Systems*. 2022. p. 1-15.

29. Xu, H.P., Xie, H.Q., Yang, D.D., Wu, Y.H. and Wang, J.R., *Novel dielectric behaviors in PVDF-based semiconductor composites*. Journal of Applied Polymer Science, 2011. **122**(5): p. 3466-3473.
30. Chen, X., Han, X. and Shen, Q.D., *PVDF-based ferroelectric polymers in modern flexible electronics*. Advanced Electronic Materials, 2017. **3**(5): p. 1600460.
31. Husain, M., Singh, R. and Pabla, B.S., *On 3D printing of PVDF composite-based sensors for biomedical applications*. National Academy Science Letters, 2022. **47**(2): p. 147-152.
32. Santos, B.P.S., Arias, J.J.R., Jorge, F.E., Santos, R.P., Fernandes, B.S., Candido, L.S., Peres, A.C.C., Chaves, E.G. and Marques, M.F.V, *PVDF containing different oxide nanoparticles for application in oil and gas pipelines*. Materials Today Communications, 2021. **26**: p. 101743.
33. Van Goethem, C., Mertens, M. and Vankelecom, I.F., *Crosslinked PVDF membranes for aqueous and extreme pH nanofiltration*. Journal of Membrane Science, 2019. **572**: p. 489-495.
34. Gül, Ç., Kocak, E.D., *Emerging applications of polymers for automobile industries*, in *Specialty Polymers*. 2023. p. 157-168.
35. Righetti, M.C., Boggioni, A., Laus, M., Antonioli, D., Sparnacci, K. and Boarino, L., *Thermal and mechanical properties of PES/PTFE composites and nanocomposites*. Journal of Applied Polymer Science, 2013. **130**(5): p. 3624-3633.
36. Wasylęczko, M., Wojciechowski, C. and Chwojnowski, A., *Polyethersulfone polymer for biomedical applications and biotechnology*. International Journal of Molecular Sciences, 2024. **25**(8): p. 4233.

37. Irfan, M., Idris, A., *Overview of PES biocompatible/hemodialysis membranes: PES–blood interactions and modification techniques*. Materials Science and Engineering: C, 2015. **56**: p. 574-592.
38. Novoselov, K.S., Geim, A.K., Morozov, S.V., Jiang, D.E., Zhang, Y., Dubonos, S.V., Grigorieva, I.V. and Firsov, A.A., *Electric field effect in atomically thin carbon films*. Science, 2004. **306**(5696): p. 666-669.
39. Geim, A.K., *Graphene: Status and Prospects*. Science 2009. **324**(5934): p. 1530-1534.
40. Noorden, R.V., *Production: Beyond sticky tape*. Nature, 2012. **483**(7389): p. S32-S33.
41. Scarpa, F., Adhikari, S. and Phani, A.S., *Effective elastic mechanical properties of single layer graphene sheets*. Nanotechnology, 2009. **20**(6): p. 065709.
42. Novoselov, K.S., Geim, A.K., Morozov, S.V., Jiang, D., Katsnelson, M.I., Grigorieva, I.V., Dubonos, S. and Firsov, A.A., *Two-dimensional gas of massless Dirac fermions in graphene*. Nature, 2005. **438**(7065): p. 197-200.
43. Sang M, S.J., Kim K, Yu KJ., *Electronic and thermal properties of graphene and recent advances in graphene based electronics applications*. Nanomaterials (Basel), 2019. **9**(3): p. 374.
44. Seol, J.H., Jo, I., Moore, A.L., Lindsay, L., Aitken, Z.H., Pettes, M.T., Li, X., Yao, Z., Huang, R., Broido, D. and Mingo, N., *Two-dimensional phonon transport in supported graphene*. Science, 2010. **328**(5975): p. 213-216.
45. Hwang, H.J., Kim, S.Y., Lee, S.K. and Lee, B.H., *Large scale graphene thermoelectric device with high power factor using gradient doping profile*. Carbon, 2023. **201**: p. 467-472.
46. Texter, J., *Graphene dispersions*. Current Opinion in Colloid & Interface Science, 2014. **19**(2): p. 163-174.

47. Tambe, P., Sharma, A., Kulkarni, H. and Panda, B., *Solvent assisted dispersion of graphene and its PVA nanocomposites coating: Processing and characterization*. Materials Today: Proceedings, 2022. **56**: p. 1383-1390.
48. Siklitskaya, A., Gacka, E., Larowska, D., Mazurkiewicz-Pawlicka, M., Malolepszy, A., Stobiński, L., Marciniak, B., Lewandowska-Andrałojć, A. and Kubas, A., *Lerf–Klinowski-type models of graphene oxide and reduced graphene oxide are robust in analyzing non-covalent functionalization with porphyrins*. Scientific Reports, 2021. **11**(1): p. 7977.
49. Nawawi, Z., Kurnia, R.F., Isa, N.F.A., Buntat, Z., Yuniarti, D.R., Jambak, M.I. and Sidik, M.A.B., *Electrical potential distribution in polymethyl methacrylate—graphene oxide nanocomposites*. Indonesia Journal of Electrical Engineering and Computer Science, 2016. **4**(2): p. 256-262.
50. Hidayah, N.M.S., Liu, W.W., Lai, C.W., Noriman, N.Z., Khe, C.S., Hashim, U. and Lee, H.C., *Comparison on graphite, graphene oxide and reduced graphene oxide: Synthesis and characterization*. AIP Conference Proceedings 2017. **1892**(1): p. 150002.
51. Chen, X., Qiu, M., Ding, H., Fu, K. and Fan, Y., *A reduced graphene oxide nanofiltration membrane intercalated by well-dispersed carbon nanotubes for drinking water purification*. Nanoscale, 2016. **8**(10): p. 5696-5705.
52. Huang, L., Chen, J., Gao, T., Zhang, M., Li, Y., Dai, L., Qu, L. and Shi, G., *Reduced graphene oxide membranes for ultrafast organic solvent nanofiltration*. Adv. Mater, 2016. **28**(39): p. 8669-8674.
53. Yang, L., Xiao, X., Shen, S., Lama, J., Hu, M., Jia, F., Han, Z., Qu, H., Huang, L., Wang, Y. and Wang, T., *Recent advances in graphene oxide membranes for nanofiltration*. ACS Appl. Nano Mater, 2022. **5**(3): p. 3121–3145

54. Yang, Y., Yang, X., Liang, L., Gao, Y., Cheng, H., Li, X., Zou, M., Ma, R., Yuan, Q. and Duan, X., *Large-area graphene-nanomesh/carbon-nanotube hybrid membranes for ionic and molecular nanofiltration*. Science, 2019. **364**(6445): p. 1057-1062.
55. Lin, L.C., Grossman, J.C., *Atomistic understandings of reduced graphene oxide as an ultrathin-film nanoporous membrane for separations*. Nature Communications, 2015. **6**(1): p. 8335.
56. Wang, Z., Ma, C., Sinquefield, S.A., Shofner, M.L. and Nair, S., *High-performance graphene oxide nanofiltration membranes for black liquor concentration*. ACS Sustainable Chemistry & Engineering, 2019. **7**(17): p. 14915-14923.
57. Lee, B.S., Lee, Y., Hwang, J.Y. and Choi, Y.C., *Structural properties of reduced graphene oxides prepared using various reducing agents*. Carbon Letters, 2015. **16**(4): p. 255-259.
58. Staudenmaier, L., *Verfahren zur darstellung der graphitsäure*. Berichte der deutschen chemischen Gesellschaft, 1898. **31**(2): p. 1481-1487.
59. Yu, H., Zhang, B., Bulin, C., Li, R. and Xing, R., *High-efficient synthesis of graphene oxide based on improved hummers method*. Scientific Reports, 2016. **6**(1): p. 1-7.
60. Poh, H.L., Šaněk, F., Ambrosi, A., Zhao, G., Sofer, Z. and Pumera, M., *Graphenes prepared by Staudenmaier, Hofmann and Hummers methods with consequent thermal exfoliation exhibit very different electrochemical properties*. Nanoscale, 2012. **4**(11): p. 3515-3522.
61. Hummers Jr, W.S., Offeman, R.E., *Preparation of graphitic oxide*. Journal of the American Chemical Society, 1958. **80**(6): p. 1339-1339.
62. Alkhouzaam, A., Qiblawey, H., , *Functional GO-based membranes for water treatment and desalination: Fabrication methods, performance and advantages. A review*. Chemosphere, 2021. **274**: p. 129853.

63. Chen, J., Yao, B., Li, C. and Shi, G., *An improved Hummers method for eco-friendly synthesis of graphene oxide*. Carbon, 2013. **64**: p. 225-229.
64. Sun, J., Yang, N., Sun, Z., Zeng, M., Fu, L., Hu, C. and Hu, S., *Fully converting graphite into graphene oxide hydrogels by preoxidation with impure manganese dioxide*. ACS Applied Materials & Interfaces, 2015. **7**(38): p. 21356-21363.
65. Yu, C., Wang, C.F. and Chen, S., *Facile access to graphene oxide from ferro-induced oxidation*. Scientific Reports, 2016. **6**(1): p. 17071.
66. Feng, X., Chen, W. and Yan, L., *Electrochemical reduction of bulk graphene oxide materials*. RSC Advances, 2016. **6**(83): p. 80106-80113.
67. Alam, S.N., Sharma, N. and Kumar, L., *Synthesis of graphene oxide (GO) by modified hummers method and its thermal reduction to obtain reduced graphene oxide (rGO)*. Graphene, 2017. **6**(1): p. 1-18.
68. Sánchez-Campos, D., Rodríguez-Lugo, V., Sánchez-Vargas, F.C., Mendoza-Anaya, D., Salinas-Rodríguez, E., Escobar-Alarcon, L. and Reyes-Valderrama, M.I., *Simple process and uncomplicated reduction of graphene oxide*. Materials Chemistry and Physics, 2020. **242**: p. 122325.
69. Díez, N., Śliwak, A., Gryglewicz, S., Grzyb, B. and Gryglewicz, G., *Enhanced reduction of graphene oxide by high-pressure hydrothermal treatment*. RSC Advances, 2015. **5**(100): p. 81831-81837.
70. Zhang, Y., Tian, J., Li, H., Wang, L., Qin, X., Asiri, A.M., Al-Youbi, A.O. and Sun, X., *Biomolecule-assisted, environmentally friendly, one-pot synthesis of CuS/reduced graphene oxide nanocomposites with enhanced photocatalytic performance*. Langmuir, 2012. **28**(35): p. 12893-12900.

71. Abdelhalim, A.O., Sharoyko, V.V., Meshcheriakov, A.A., Martynova, S.D., Ageev, S.V., Iurev, G.O., Al Mulla, H., Petrov, A.V., Solovtsova, I.L., Vasina, L.V. and Murin, I.V., *Reduction and functionalization of graphene oxide with L-cysteine: Synthesis, characterization and biocompatibility*. *Nanomedicine: Nanotechnology, Biology and Medicine*, 2020. **29**: p. 102284.
72. Bansal, K., Singh, J. and Dhaliwal, A.S. *Synthesis and characterization of Graphene Oxide and its reduction with different reducing agents*. in *In IOP Conference Series: Materials Science and Engineering*. 2022. IOP Publishing.
73. Unnikrishnan, A., Alexander, L.K., *The concentration-dependent effect of NaOH on graphene oxide: Revisited as a reducing agent*. *Journal of Physics and Chemistry of Solids*, 2024. **190**: p. 111978.
74. Song, X., Zambare, R.S., Qi, S., Sowrirajalu, B.N., James Selvaraj, A.P., Tang, C.Y. and Gao, C., *Charge-gated ion transport through polyelectrolyte intercalated amine reduced graphene oxide membranes*. *ACS Applied Materials & interfaces*, 2017. **9**(47): p. 41482-41495.
75. Zhu, Y., Cai, W., Piner, R.D., Velamakanni, A. and Ruoff, R.S., *Transparent self-assembled films of reduced graphene oxide platelets*. *Applied Physics Letters*, 2009. **95**(10).
76. Su, Y., Kravets, V.G., Wong, S.L., Waters, J., Geim, A.K. and Nair, R.R., *Impermeable barrier films and protective coatings based on reduced graphene oxide*. *Nature Communications*, 2014. **5**(1): p. 4843.
77. Zhang, W., Xu, H., Xie, F., Ma, X., Niu, B., Chen, M., Zhang, H., Zhang, Y. and Long, D., *General synthesis of ultrafine metal oxide/reduced graphene oxide nanocomposites for ultrahigh-flux nanofiltration membrane*. *Nature Communications*, 2022. **13**(1): p. 471.

78. Safarpour, M., Vatanpour, V. and Khataee, A., *Preparation and characterization of graphene oxide/TiO₂ blended PES nanofiltration membrane with improved antifouling and separation performance*. *Desalination*, 2016. **393**: p. 65-78.
79. Rashidi, F., Kevlich, N.S., Sinquefield, N.A., Shofner, M.L., and Nair, S., *Graphene oxide membranes in extreme operating environments: concentration of kraft black liquor by lignin retention*. *ACS Sustainable Chemistry & Engineering*, 2017. **5**(1): p. 1002-1009.
80. Wang, Z., Ma, C., Sinquefield, S.A., Shofner, M.L. and Nair, S., *Graphene oxide nanofiltration membranes for desalination under realistic conditions*. *Nature Sustainability* 2021. **4**: p. 402-408.
81. Han, Y., Xu, Z. and Gao, C., *Ultrathin graphene nanofiltration membrane for water purification*. *Advanced Functional Materials*, 2013. **23**(29): p. 3693-3700.
82. Wang, E.N., Karnik., R, *Graphene cleans up water*. *Nature Nanotechnology*, 2012. **7**(9): p. 552-554.
83. Gass, M.H., Bangert, U., Bleloch, A.L., Wang, P., Nair, R.R. and Geim, A.K., *Free-standing graphene at atomic resolution*. *Nature Nanotechnology*, 2008. **3**(11): p. 676–681.
84. Ha, S.H., Jeong, Y.S. and Lee, Y.J., *Free standing reduced graphene oxide film cathodes for lithium ion batteries*. *ACS Applied Materials & Interfaces*, 2013. **5**(23): p. 12295-12303.
85. Zhao, S., Li, M., Wu, X., Yu, S.H., Zhang, W., Luo, J., Wang, J., Geng, Y., Gou, Q. and Sun, K., *Graphene-based free-standing bendable films: designs, fabrications, and applications*. *Materials Today Advances*, 2020. **6**: p. 100060.
86. Xia, Q., Zhang, Z., Liu, Y. and Leng, J., *Buckypaper and its composites for aeronautic applications*. *Composites Part B: Engineering*, 2020. **199**: p. 108231.

87. Liu, H., Wang, H. and Zhang, X., *Facile Fabrication of Freestanding Ultrathin Reduced Graphene Oxide Membranes for Water Purification*. *Adv. Mater*, 2015. **27**(2): p. 249-254.
88. Wang, B., Luo, D., Li, Z., Kwon, Y., Wang, M., Goo, M., Jin, S., Huang, M., Shen, Y., Shi, H. and Ding, F., *Camphor-enabled transfer and mechanical testing of centimeter-scale ultrathin films*. *Advanced Materials*, 2018. **30**(28): p. 1800888.
89. Kang, S.H., Fang, T.H., Hong, Z.H. and Chuang, C.H., *Mechanical properties of free-standing graphene oxide*. *Diamond and Related Materials*, 2013. **38**: p. 73-78.
90. Karthick, R., Chen, F., *Free-standing graphene paper for energy application: Progress and future scenarios*. *Carbon*, 2019. **150**: p. 292-310.
91. Yang, H., Cao, Y., He, J., Zhang, Y., Jin, B., Sun, J.L., Wang, Y. and Zhao, Z., *Highly conductive free-standing reduced graphene oxide thin films for fast photoelectric devices*. *Carbon*, 2017. **115**: p. 561-570.
92. Zhuang, P., Fu, H., Xu, N., Li, B., Xu, J. and Zhou, L., *Free-standing reduced graphene oxide (rGO) membrane for salt-rejecting solar desalination via size effect*. *Nanophotonics*, 2020. **9**(15): p. 4601-460.
93. Baysal, T., Güvensoy-Morkoyun, A., Tantekin-Ersolmaz, Ş.B. and Velioglu, S., *Methanol recovery: potential of nanolaminate organic solvent nanofiltration (OSN) membranes*. *Nanoscale*, 2024. **16**(7): p. 3393-3416.
94. Sui, X., Yuan, Z., Liu, C., Wei, L., Xu, M., Liu, F., Montoya, A., Goh, K. and Chen, Y., *Graphene oxide laminates intercalated with 2D covalent-organic frameworks as a robust nanofiltration membrane*. *J. Mater. Chem.*, 2020. **8**(19): p. 9713-9725.
95. Krishnamoorthi R., B.F.S., Mazlan N.A., Chen S., Radacsi N., Yang S., Yoon Y., Huang Yi., *Tuning the interlayer spacing of graphene oxide membrane via surfactant intercalation for ultrafast nanofiltration*. *Journal of Membrane Science* 2024: p. 122942.

96. Chen, L., Li, N., Wen, Z., Zhang, L., Chen, Q., Chen, L., Si, P., Feng, J., Li, Y., Lou, J. and Ci, L., *Graphene oxide based membrane intercalated by nanoparticles for high performance nanofiltration application*. Chemical Engineering Journal, 2018. **347**: p. 12-18.
97. Lin, H., Li, Y. and Zhu, J., *Graphite oxide/boron nitride hybrid membranes: The role of cross-plane laminar bonding for a durable membrane with large water flux and high rejection rate*. Journal of Membrane Science, 2020. **593**: p. 117401.
98. Sonker, M., Zaw, K.S.K., Dhruve, H.P., Abbaszadeh, M., Garell, M.P., Rickman, M., Salerno, M.B., Hatzell, M.C., Shofner, M.L., Sankar, N., *Structure-property relationships of intercalated reduced graphene oxide membranes for petroleum desalter Water processing*. Paper in Preparation.
99. Roylance, D. *Stress-Strain curves*. Massachusetts Institute of Technology study Cambridge, 2001. **15**.
100. Shuman, D.J., A.L.M. Costa, and M.S. Andrade, *Calculating the elastic modulus from nanoindentation and microindentation reload curves*. Materials Characterization, 2007. **58**(4): p. 380-389.
101. Pharr, G.M., Oliver, W. C., *Measurement of thin-film mechanical-properties using nanoindentation*. MRS Bulletin, 1992. **17**(7): p. 28-33.
102. Sawa, T. and K. Tanaka, *Simplified method for analyzing nanoindentation data and evaluating performance of nanoindentation instruments*. Journal of Materials Research, 2001. **16**(11): p. 3084-3096.
103. Němeček, J., Lukeš, J., *High-speed mechanical mapping of blended cement pastes and its comparison with standard modes of nanoindentation*. Materials Today Communications, 2020. **23**: p. 100806.

104. Batakliiev, T., Ivanov, E., Angelov, V., Spinelli, G. and Kotsilkova, R., *Advanced nanomechanical characterization of biopolymer films containing GNPs and MWCNTs in hybrid composite structure*. *Nanomaterials*, 2022. **12**(4): p. 709.
105. Cordill, M.J., Taylor, A., Schalko, J. and Dehm, G., *Fracture and Delamination of Chromium Thin Films on Polymer Substrates*. *Metallurgical and Materials Transactions a-Physical Metallurgy and Materials Science*, 2010. **41a**(4): p. 870-875.
106. Croft, Z.L., Xu Z., Cao, K., Guo, D., Sreeharikesan, S., Thompson, C., Zeltzer, G., Liu, G., *Can the voigt model be directly used for determining the modulus of graphene in laminate thin films?* *ACS Appl. Polym. Mater.* , 2022: p. 394-402.
107. Bull, S.J., *A simple method for the assessment of the contact modulus for coated systems*. *Philosophical Magazine*, 2014. **95**: p. 16-18.
108. Mouritz, A.P., *Review of z-pinned composite laminates*. *Composites Part A: Applied Science and Manufacturing*, 2007. **38**(12): p. 2383-2397.
109. Li, M., Che, Z., Wang, S., Zhou, Y., Fu, H., Gu, Y., Zhang, W., *Tuning interlaminar fracture toughness of fine z-pin reinforced polymer composite*. *Materials & Design*, 2021. **212**: p. 110293.
110. Humood, M., Asif, A., Guin, T., Polychronopoulou, K., Grunlan, J.C. and Polycarpou, A.A., *Nanoindentation and nanoscratch of sub-micron polymer nanocomposite films on compliant substrate*. *Thin Solid Films*, 2021. **736**: p. 138905.
111. Beake, B.D., Harris, A.J. and Liskiewicz, T.W., *Review of recent progress in nanoscratch testing*. *Tribology-Materials, Surfaces & Interfaces*, 2013. **7**(2): p. 87-96.
112. Shokrieh, M.M., Hosseinkhani, M.R., Naimi-Jamal, M.R. and Tourani, H.J.P.T., *Nanoindentation and nanoscratch investigations on graphene-based nanocomposites*. *Polymer Testing*, 2013. **32**(1): p. 45-51.

113. Laugier, M., *The development of the scratch test technique for the determination of the adhesion of coatings*. Thin Solid Films, 1981. **76**(3): p. 289-294.
114. Chang, S.Y., Huang, Y.C., *Analyses of interface adhesion between porous SiO₂ low-k film and SiC/SiN layers by nanoindentation and nanoscratch tests*. Microelectronic Engineering, 2007. **84**(2): p. 319-327.
115. Zhang, S., Guo, X., Jin, Z., Kang, R., Guo, D. and Tang, W.C., *Surface morphologies and corresponding hardness evolution during nanoscratching*. Journal of Materials Research and Technology, 2020. **9**(3): p. 3179-3189.
116. Mallikarjunachari, G., Ghosh, P., *Analysis of strength and response of polymer nano thin film interfaces applying nanoindentation and nanoscratch techniques*. Polymer, 2016. **90**: p. 53-66.